DESY 07-115 ISSN 0418-9833
August 2007

Dijet Cross Sections and Parton Densities in Diffractive DIS at HERA

H1 Collaboration

Abstract

Differential dijet cross sections in diffractive deep-inelastic scattering are measured with the H1 detector at HERA using an integrated luminosity of 51.5 pb^{-1}. The selected events are of the type $ep \rightarrow eXY$, where the system X contains at least two jets and is well separated in rapidity from the low mass proton dissociation system Y. The dijet data are compared with QCD predictions at next-to-leading order based on diffractive parton distribution functions previously extracted from measurements of inclusive diffractive deep-inelastic scattering. The prediction describes the dijet data well at low and intermediate $z_{I\!P}$ (the fraction of the momentum of the diffractive exchange carried by the parton entering the hard interaction) where the gluon density is well determined from the inclusive diffractive data, supporting QCD factorisation. A new set of diffractive parton distribution functions is obtained through a simultaneous fit to the diffractive inclusive and dijet cross sections. This allows for a precise determination of both the diffractive quark and gluon distributions in the range $0.05 < z_{I\!P} < 0.9$. In particular, the precision on the gluon density at high momentum fractions is improved compared to previous extractions.

Submitted to the Journal of High Energy Physics

A. Aktas[11], C. Alexa[5], V. Andreev[25], T. Anthonis[4], B. Antunovic[26], S. Aplin[11], A. Asmone[33], A. Astvatsatourov[4], S. Backovic[30], A. Baghdasaryan[38], P. Baranov[25], E. Barrelet[29], W. Bartel[11], S. Baudrand[27], M. Beckingham[11], K. Begzsuren[35], O. Behnke[14], O. Behrendt[8], A. Belousov[25], N. Berger[40], J.C. Bizot[27], M.-O. Boenig[8], V. Boudry[28], I. Bozovic-Jelisavcic[2], J. Bracinik[26], G. Brandt[14], M. Brinkmann[11], V. Brisson[27], D. Bruncko[16], F.W. Büsser[12], A. Bunyatyan[13,38], G. Buschhorn[26], L. Bystritskaya[24], A.J. Campbell[11], K.B. Cantun Avila[22], F. Cassol-Brunner[21], K. Cerny[32], V. Cerny[16,47], V. Chekelian[26], A. Cholewa[11], J.G. Contreras[22], J.A. Coughlan[6], G. Cozzika[10], J. Cvach[31], J.B. Dainton[18], K. Daum[37,43], M. Deak[11], Y. de Boer[24], B. Delcourt[27], M. Del Degan[40], J. Delvax[4], A. De Roeck[11,45], E.A. De Wolf[4], C. Diaconu[21], V. Dodonov[13], A. Dubak[30,46], G. Eckerlin[11], V. Efremenko[24], S. Egli[36], R. Eichler[36], F. Eisele[14], A. Eliseev[25], E. Elsen[11], S. Essenov[24], A. Falkiewicz[7], P.J.W. Faulkner[3], L. Favart[4], A. Fedotov[24], R. Felst[11], J. Feltesse[10,48], J. Ferencei[16], L. Finke[11], M. Fleischer[11], A. Fomenko[25], G. Franke[11], T. Frisson[28], E. Gabathuler[18], J. Gayler[11], S. Ghazaryan[38], S. Ginzburgskaya[24], A. Glazov[11], I. Glushkov[39], L. Goerlich[7], M. Goettlich[12], N. Gogitidze[25], S. Gorbounov[39], M. Gouzevitch[28], C. Grab[40], T. Greenshaw[18], B.R. Grell[11], G. Grindhammer[26], S. Habib[12,50], D. Haidt[11], M. Hansson[20], G. Heinzelmann[12], C. Helebrant[11], R.C.W. Henderson[17], H. Henschel[39], G. Herrera[23], M. Hildebrandt[36], K.H. Hiller[39], D. Hoffmann[21], R. Horisberger[36], A. Hovhannisyan[38], T. Hreus[4,44], M. Jacquet[27], M.E. Janssen[11], X. Janssen[4], V. Jemanov[12], L. Jönsson[20], D.P. Johnson[4,†], A.W. Jung[15], H. Jung[11], M. Kapichine[9], J. Katzy[11], I.R. Kenyon[3], C. Kiesling[26], M. Klein[18], C. Kleinwort[11], T. Klimkovich[11], T. Kluge[11], A. Knutsson[20], V. Korbel[11], P. Kostka[39], M. Kraemer[11], K. Krastev[11], J. Kretzschmar[39], A. Kropivnitskaya[24], K. Krüger[15], M.P.J. Landon[19], W. Lange[39], G. Laštovička-Medin[30], P. Laycock[18], A. Lebedev[25], G. Leibenguth[40], V. Lendermann[15], S. Levonian[11], G. Li[27], L. Lindfeld[41], K. Lipka[12], A. Liptaj[26], B. List[12], J. List[11], N. Loktionova[25], R. Lopez-Fernandez[23], V. Lubimov[24], A.-I. Lucaci-Timoce[11], L. Lytkin[13], A. Makankine[9], E. Malinovski[25], P. Marage[4], Ll. Marti[11], M. Martisikova[11], H.-U. Martyn[1], S.J. Maxfield[18], A. Mehta[18], K. Meier[15], A.B. Meyer[11], H. Meyer[11], H. Meyer[37], J. Meyer[11], V. Michels[11], S. Mikocki[7], I. Milcewicz-Mika[7], A. Mohamed[18], F. Moreau[28], A. Morozov[9], J.V. Morris[6], M.U. Mozer[14], K. Müller[41], P. Murín[16,44], K. Nankov[34], B. Naroska[12], Th. Naumann[39], P.R. Newman[3], C. Niebuhr[11], A. Nikiforov[26], G. Nowak[7], K. Nowak[41], M. Nozicka[39], R. Oganezov[38], B. Olivier[26], J.E. Olsson[11], S. Osman[20], D. Ozerov[24], V. Palichik[9], I. Panagoulias[l,11,42], M. Pandurovic[2], Th. Papadopoulou[l,11,42], C. Pascaud[27], G.D. Patel[18], H. Peng[11], E. Perez[10], D. Perez-Astudillo[22], A. Perieanu[11], A. Petrukhin[24], I. Picuric[30], S. Piec[39], D. Pitzl[11], R. Plačakytė[11], R. Polifka[32], B. Povh[13], T. Preda[5], P. Prideaux[18], V. Radescu[11], A.J. Rahmat[18], N. Raicevic[30], T. Ravdandorj[35], P. Reimer[31], C. Risler[11], E. Rizvi[19], P. Robmann[41], B. Roland[4], R. Roosen[4], A. Rostovtsev[24], Z. Rurikova[11], S. Rusakov[25], F. Salvaire[11], D.P.C. Sankey[6], M. Sauter[40], E. Sauvan[21], S. Schmidt[11], S. Schmitt[11], C. Schmitz[41], L. Schoeffel[10], A. Schöning[40], H.-C. Schultz-Coulon[15], F. Sefkow[11], R.N. Shaw-West[3], I. Sheviakov[25], L.N. Shtarkov[25], T. Sloan[17], I. Smiljanic[2], P. Smirnov[25], Y. Soloviev[25], D. South[8], V. Spaskov[9], A. Specka[28], Z. Staykova[11], M. Steder[11], B. Stella[33], J. Stiewe[15], U. Straumann[41], D. Sunar[4], T. Sykora[4], V. Tchoulakov[9], G. Thompson[19], P.D. Thompson[3], T. Toll[11], F. Tomasz[16], T.H. Tran[27], D. Traynor[19], T.N. Trinh[21], P. Truöl[41], I. Tsakov[34], B. Tseepeldorj[35], G. Tsipolitis[11,42], I. Tsurin[39], J. Turnau[7], E. Tzamariudaki[26], K. Urban[15], D. Utkin[24], A. Valkárová[32], C. Vallée[21], P. Van Mechelen[4], A. Vargas Trevino[11], Y. Vazdik[25], S. Vinokurova[11], V. Volchinski[38], G. Weber[12], R. Weber[40], D. Wegener[8], C. Werner[14],

M. Wessels[11], Ch. Wissing[11], R. Wolf[14], E. Wünsch[11], S. Xella[41], V. Yeganov[38], J. Žáček[32], J. Zálešák[31], Z. Zhang[27], A. Zhelezov[24], A. Zhokin[24], Y.C. Zhu[11], T. Zimmermann[40], H. Zohrabyan[38], and F. Zomer[27]

[1] *I. Physikalisches Institut der RWTH, Aachen, Germany*[a]
[2] *Vinca Institute of Nuclear Sciences, Belgrade, Serbia*
[3] *School of Physics and Astronomy, University of Birmingham, Birmingham, UK*[b]
[4] *Inter-University Institute for High Energies ULB-VUB, Brussels; Universiteit Antwerpen, Antwerpen; Belgium*[c]
[5] *National Institute for Physics and Nuclear Engineering (NIPNE) , Bucharest, Romania*
[6] *Rutherford Appleton Laboratory, Chilton, Didcot, UK*[b]
[7] *Institute for Nuclear Physics, Cracow, Poland*[d]
[8] *Institut für Physik, Universität Dortmund, Dortmund, Germany*[a]
[9] *Joint Institute for Nuclear Research, Dubna, Russia*
[10] *CEA, DSM/DAPNIA, CE-Saclay, Gif-sur-Yvette, France*
[11] *DESY, Hamburg, Germany*
[12] *Institut für Experimentalphysik, Universität Hamburg, Hamburg, Germany*[a]
[13] *Max-Planck-Institut für Kernphysik, Heidelberg, Germany*
[14] *Physikalisches Institut, Universität Heidelberg, Heidelberg, Germany*[a]
[15] *Kirchhoff-Institut für Physik, Universität Heidelberg, Heidelberg, Germany*[a]
[16] *Institute of Experimental Physics, Slovak Academy of Sciences, Košice, Slovak Republic*[f]
[17] *Department of Physics, University of Lancaster, Lancaster, UK*[b]
[18] *Department of Physics, University of Liverpool, Liverpool, UK*[b]
[19] *Queen Mary and Westfield College, London, UK*[b]
[20] *Physics Department, University of Lund, Lund, Sweden*[g]
[21] *CPPM, CNRS/IN2P3 - Univ. Mediterranee, Marseille - France*
[22] *Departamento de Fisica Aplicada, CINVESTAV, Mérida, Yucatán, México*[j]
[23] *Departamento de Fisica, CINVESTAV, México*[j]
[24] *Institute for Theoretical and Experimental Physics, Moscow, Russia*
[25] *Lebedev Physical Institute, Moscow, Russia*[e]
[26] *Max-Planck-Institut für Physik, München, Germany*
[27] *LAL, Univ Paris-Sud, CNRS/IN2P3, Orsay, France*
[28] *LLR, Ecole Polytechnique, IN2P3-CNRS, Palaiseau, France*
[29] *LPNHE, Universités Paris VI and VII, IN2P3-CNRS, Paris, France*
[30] *Faculty of Science, University of Montenegro, Podgorica, Montenegro*[e]
[31] *Institute of Physics, Academy of Sciences of the Czech Republic, Praha, Czech Republic*[h]
[32] *Faculty of Mathematics and Physics, Charles University, Praha, Czech Republic*[h]
[33] *Dipartimento di Fisica Università di Roma Tre and INFN Roma 3, Roma, Italy*
[34] *Institute for Nuclear Research and Nuclear Energy, Sofia, Bulgaria*[e]
[35] *Institute of Physics and Technology of the Mongolian Academy of Sciences , Ulaanbaatar, Mongolia*
[36] *Paul Scherrer Institut, Villigen, Switzerland*
[37] *Fachbereich C, Universität Wuppertal, Wuppertal, Germany*
[38] *Yerevan Physics Institute, Yerevan, Armenia*
[39] *DESY, Zeuthen, Germany*
[40] *Institut für Teilchenphysik, ETH, Zürich, Switzerland*[i]

[41] *Physik-Institut der Universität Zürich, Zürich, Switzerland*[i]

[42] *Also at Physics Department, National Technical University, Zografou Campus, GR-15773 Athens, Greece*
[43] *Also at Rechenzentrum, Universität Wuppertal, Wuppertal, Germany*
[44] *Also at University of P.J. Šafárik, Košice, Slovak Republic*
[45] *Also at CERN, Geneva, Switzerland*
[46] *Also at Max-Planck-Institut für Physik, München, Germany*
[47] *Also at Comenius University, Bratislava, Slovak Republic*
[48] *Also at DESY and University Hamburg, Helmholtz Humboldt Research Award*
[50] *Supported by a scholarship of the World Laboratory Björn Wiik Research Project*
[†] *Deceased*

[a] *Supported by the Bundesministerium für Bildung und Forschung, FRG, under contract numbers 05 H1 1GUA /1, 05 H1 1PAA /1, 05 H1 1PAB /9, 05 H1 1PEA /6, 05 H1 1VHA /7 and 05 H1 1VHB /5*
[b] *Supported by the UK Particle Physics and Astronomy Research Council, and formerly by the UK Science and Engineering Research Council*
[c] *Supported by FNRS-FWO-Vlaanderen, IISN-IIKW and IWT and by Interuniversity Attraction Poles Programme, Belgian Science Policy*
[d] *Partially Supported by Polish Ministry of Science and Higher Education, grant PBS/DESY/70/2006*
[e] *Supported by the Deutsche Forschungsgemeinschaft*
[f] *Supported by VEGA SR grant no. 2/7062/ 27*
[g] *Supported by the Swedish Natural Science Research Council*
[h] *Supported by the Ministry of Education of the Czech Republic under the projects LC527 and INGO-1P05LA259*
[i] *Supported by the Swiss National Science Foundation*
[j] *Supported by CONACYT, México, grant 400073-F*
[l] *This project is co-funded by the European Social Fund (75%) and National Resources (25%) - (EPEAEK II) - PYTHAGORAS II*

1 Introduction

Hadron-hadron collisions proceed predominantly via soft interactions to which perturbative Quantum Chromodynamics (QCD) cannot be applied. In a sizeable fraction of these soft processes the colliding hadrons remain intact or merely dissociate to larger mass states with the same quantum numbers. These "diffractive processes" dominate the behaviour of the total cross section at high energy and are phenomenologically described by the exchange of the pomeron trajectory, which carries the quantum numbers of the vacuum. The parton composition of this diffractive exchange is, however, not well known.

Processes of the type $ep \to eXp$ have been studied in detail at HERA. These processes can be pictured as $\gamma^{\star}p$ scattering, where the virtual photon interacts with a diffractive exchange and dissociates to produce a system X. In QCD a hard scattering collinear factorisation theorem [1] predicts that the cross section for diffractive deep-inelastic ep scattering (DIS) factorises into a set of universal diffractive parton distribution functions (DPDFs) of the proton and process-dependent hard scattering coefficients. DPDFs have been determined through QCD fits to the measured cross sections of inclusive diffractive scattering at HERA [2–15].

If QCD factorisation is fulfilled, next-to-leading order (NLO) QCD calculations based on DPDFs such as those extracted in [5] should be able to predict the production rates of more exclusive diffractive processes such as dijet and open charm production. Previous measurements of such exclusive cross sections in DIS [16–23] support QCD factorisation since they can be reasonably well described using the DPDFs determined from inclusive diffractive scattering. Diffractive dijet and charm production proceed mainly via boson gluon fusion (BGF, depicted in figure 1) and are therefore mainly sensitive to the diffractive gluon density. It was recently shown [5] that inclusive diffractive scattering data do not constrain the diffractive gluon density well at high momentum fractions. Thus stringent tests of factorisation can only be performed at low momentum fractions. However, the gluon density at high momentum fractions is particularly relevant for the estimation of cross sections for several important processes at the LHC [24]. Measurements of diffractive dijet production can directly constrain the diffractive gluon density at high momentum fractions, extending the kinematic range of reliably determined diffractive parton densities.

In this paper, a new measurement of diffractive dijet cross sections in deep-inelastic scattering is presented, based on data collected with the H1 detector at HERA in the years 1999 and 2000. These are the first HERA diffractive DIS dijet data with $E_p = 920$ GeV. Jets are defined using the inclusive k_T algorithm [25]. The resulting dijet cross sections are compared to NLO QCD predictions based on DPDFs previously extracted [5] from inclusive diffractive ep scattering at H1. For the first time, a combined NLO QCD fit is performed to the differential dijet cross sections and the inclusive diffractive cross section data in order to determine a new set of DPDFs.

2 Kinematics

The dominant process leading to the production of dijets in diffractive DIS is depicted in figure 1. The incoming proton of four-momentum P interacts with the positron of four-momen-

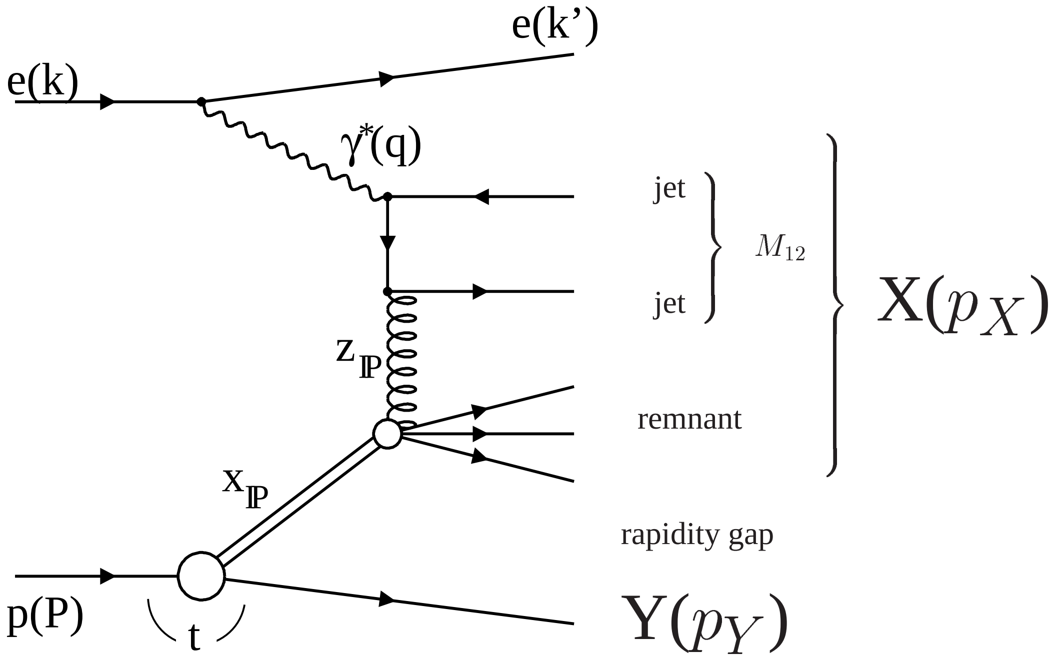

Figure 1: Leading order diagram for diffractive dijet production in DIS.

tum k via the exchange of a virtual photon with four-momentum q. The DIS kinematic variables are defined as

$$Q^2 \equiv -q^2, \qquad x \equiv \frac{-q^2}{2P \cdot q}, \qquad y \equiv \frac{P \cdot q}{P \cdot k},$$

where Q^2 is the photon virtuality, x is the longitudinal momentum fraction of the proton carried by the struck quark and y is the inelasticity of the process. These quantities are connected by the relation

$$Q^2 = xys,$$

where s denotes the fixed ep centre-of-mass energy squared.

The hadronic final state of the events is divided into two systems X and Y, separated by the largest gap in the rapidity distribution of the hadrons relative to the collision axis in the $\gamma^\star p$ centre of mass system. The diffractive scattering is described in terms of the variables

$$t \equiv (P - p_Y)^2, \quad x_{I\!P} \equiv \frac{q \cdot (P - p_Y)}{q \cdot P}, \quad \beta \equiv x/x_{I\!P},$$

with p_Y representing the four-momentum of the system Y. Here t is the squared four-momentum transfer at the proton vertex and $x_{I\!P}$ is the fraction of the proton's longitudinal momentum transferred to the system X. The fractional longitudinal momentum of the diffractive exchange carried by the parton which enters the hard interaction with four-momentum v is given by

$$z_{I\!P} = \frac{q \cdot v}{q \cdot (P - p_Y)}.$$

3 Experimental Procedure

3.1 H1 Detector

A detailed description of the H1 detector can be found in [26–28]. Here, a brief account of the components most relevant to the present analysis is given. The origin of the H1 coordinate system is the nominal ep interaction point. The direction of the proton beam defines the positive z–axis (forward direction). Transverse momenta are measured in the x–y plane. Polar (θ) and azimuthal (ϕ) angles are measured with respect to this reference system. The pseudorapidity is defined as $\eta = -\ln\tan(\theta/2)$.

The ep interaction region is surrounded by a two-layered silicon strip detector [29] and two large concentric drift chambers, operated inside a 1.16 T solenoidal magnetic field. Charged particle momenta are measured in the pseudorapidity range $-1.5 < \eta < 1.5$ with a resolution of $\sigma(p_T)/p_T = 0.005\, p_T/\text{GeV} \oplus 0.015$. The central tracking detectors also provide triggering information based on track segments measured in the r-ϕ plane of the central jet chambers and on the z position of the event vertex obtained from the double layers of two multi-wire proportional chambers. A finely segmented electromagnetic and hadronic liquid argon (LAr) calorimeter [30] covers the range $-1.5 < \eta < 3.4$. The energy resolution is $\sigma/E = 0.11/\sqrt{E/\mathrm{GeV}}$ for electromagnetic showers and $\sigma/E = 0.50/\sqrt{E/\mathrm{GeV}}$ for hadrons, as measured in test beams [31]. A lead/scintillating fibre calorimeter (SPACAL) [28] covers the backward region $-4 < \eta < -1.4$. Its main purpose is the detection of scattered positrons.

The luminosity is measured via the Bethe-Heitler Bremsstrahlung process $ep \to ep\gamma$, the final state photon being detected in a crystal calorimeter at $z = -103$ m.

The Forward Muon Detector (FMD) and the Proton Remnant Tagger (PRT) are sensitive to the energy flow in the forward region. They are used to efficiently reject events which do not exhibit a rapidity gap between the X system and the proton dissociation system Y. The FMD is located at $z = 6.5$ m and covers a pseudorapidity range of $1.9 < \eta < 3.7$. It may also detect particles produced at larger η due to secondary scattering within the beam pipe. The PRT consists of a set of scintillators surrounding the beam pipe at $z = 26$ m and covers the region $6 < \eta < 7.5$.

3.2 Event Selection

The data used in this analysis correspond to an integrated luminosity of 51.5 pb^{-1} taken in the 1999 and 2000 running periods, in which HERA collided protons of 920 GeV energy with positrons of 27.5 GeV. The data are collected using a trigger which requires the scattered positron to be detected in the SPACAL calorimeter and at least one track of transverse momentum above $0.8\ \mathrm{GeV}$ to be recorded in the central jet chamber. In the off-line analysis, the scattered positron is selected as an electromagnetic SPACAL cluster with an energy $E_e > 8$ GeV and polar angle $156^\circ < \theta_e < 176^\circ$. These requirements are well matched to the chosen kinematic range of $4 < Q^2 < 80\ \mathrm{GeV}^2$ and $0.1 < y < 0.7$. Background from photoproduction, where the positron scatters unobserved at small angles and a particle from the hadronic final state is misidentified as the scattered positron, is suppressed by the requirement that the difference between the total energy and longitudinal momentum reconstructed in the detector, $E - p_z$, must be larger than $35\ \mathrm{GeV}$. Background not related to ep collisions is reduced by restricting the z position of the event vertex to lie within 35 cm of the average ep interaction point.

Diffractive events are selected by the absence of hadronic activity above noise threshold in the most forward part of the LAr calorimeter ($\eta > 3.2$) and in the FMD and PRT. This selection ensures that the rapidity gap between the systems X and Y spans more than four units between $\eta = 3.2$ and 7.5. In addition the restriction $x_{I\!P} < 0.03$ is imposed to limit the contribution from secondary reggeon exchanges and to ensure good acceptance.

The hadronic system X is measured in the LAr and SPACAL calorimeters and the central tracking system. Calorimeter cluster energies and track momenta are combined into hadronic objects using an algorithm which avoids double counting [32]. Jets are formed from the hadronic objects, using the inclusive k_T cluster algorithm [25] with a distance parameter of unity in the photon-proton rest frame. At least two jets are required with transverse momenta in the $\gamma^\star p$ centre of mass frame of $p^\star_{T,jet1} > 5.5$ GeV and $p^\star_{T,jet2} > 4$ GeV for the leading and sub-leading jet, respectively. Asymmetric cuts on the jet transverse momenta are chosen to facilitate comparisons with NLO QCD predictions. The axes of the jets are required to lie within the region $-1.0 < \eta_{jet} < 2.0$ in the laboratory frame, well within the acceptance of the LAr calorimeter. After all cuts 2723 diffractive dijet events are selected.

3.3 Kinematic Reconstruction

The energy E_e and polar angle θ_e of the scattered positron are measured using the SPACAL and the reconstructed vertex position. The inelasticity y and photon virtuality Q^2 are determined according to

$$y = 1 - \frac{E_e}{E_e^0}\sin^2\frac{\theta_e}{2},$$
$$Q^2 = 4E_eE_e^0\cos^2\frac{\theta_e}{2},$$

where E_e^0 is the positron beam energy. The energy and momentum of the hadronic system X are reconstructed from the observed hadronic objects and the invariant mass M_X is computed from this information. The invariant mass of the dijet system is given by

$$M_{12} \equiv \sqrt{(p_{jet1} + p_{jet2})^2},$$

with p_{jet1} and p_{jet2} being the four-momenta of the leading and sub-leading jet, respectively. The observables $x_{I\!P}$ and $z_{I\!P}$ are reconstructed according to

$$x_{I\!P} = \frac{M_X^2 + Q^2}{ys},$$
$$z_{I\!P} = \frac{M_{12}^2 + Q^2}{M_X^2 + Q^2}.$$

3.4 Monte Carlo Simulations and Fixed Order QCD Predictions

Monte Carlo simulations are used in the analysis to correct the data for detector effects. For events generated with Monte Carlo programs, the H1 detector response is simulated in detail using GEANT [33] and the events are subjected to the same analysis as the data. Events are generated using the RAPGAP program [34] which simulates the process $ep \to eXp$, assuming proton vertex factorisation (see section 5.2). Leading order matrix elements for the hard QCD sub-process are convoluted with DPDFs, taken at the factorisation scale $\mu_f = \sqrt{\hat{p}_T^2 + Q^2}$, where $\hat{p}_T$ is the transverse momentum of the emerging hard partons relative to the collision axis in the $\gamma^\star p$ centre of mass frame. A preliminary version of the 'H1 2006 DPDF' fit [35] is used to simulate pomeron and sub-leading reggeon exchanges. Higher order effects are simulated using parton showers [36] in the leading logarithm approximation. The Lund string model [37,38] is used for hadronisation. QED radiative corrections are applied using the HERACLES program [39]. Processes with a resolved virtual photon are also included, with the structure of the photon given by the SAS-2D parameterisation [40].

The background due to non-diffractive deep-inelastic scattering is estimated and accounted for using the RAPGAP Monte Carlo program in its inclusive mode. The parameters are chosen to be similar to the ones used for the generation of the diffractive sample discussed above. The inclusive simulation uses the CTEQ5L parton densities of the proton [41].

In diffractive DIS measurements using the present technique the system Y does not necessarily consist only of a single proton, but may also be a low mass dissociative system. The DIFFVM program [42] includes a sophisticated treatment of the dissociating proton. It is used to study the response of the forward detectors to low mass proton dissociation systems ($m_p < M_Y < 5$ GeV). The non-resonant part of the M_Y distribution is modelled with $d\sigma/dM_Y^2 \propto (1/M_Y^2)^{1.08}$, while the t dependence follows an exponential decrease: $d\sigma/dt \propto e^{bt}$ with $b = 1.6\ \mathrm{GeV}^{-2}$. This parameterisation is motivated by measurements of diffractive vector meson production at H1 [43]. Proton dissociation processes with $M_Y > 5$ GeV are included in the treatment of non-diffractive background with RAPGAP as discussed above.

NLO QCD predictions for the dijet cross sections are calculated at the parton level using the NLOJET++ program [44] in slices of $x_{I\!P}$, assuming proton vertex factorisation. The resulting cross sections are converted to the stable hadron level by factors extracted from the RAPGAP Monte Carlo model in the diffractive mode. The renormalisation and factorisation scales are set to $\mu_r = \mu_f = \sqrt{p_{T,jet1}^{\star 2} + Q^2}$, where $p_{T,jet1}^\star$ is the transverse momentum of the leading jet in the $\gamma^\star p$ centre of mass frame. The NLOJET++ calculation uses parton densities obtained from a NLO QCD analysis of inclusive diffractive scattering at H1 [5]. That publication provides two

DIS Selection	$4 < Q^2 < 80\ \mathrm{GeV}^2$ $0.1 < y < 0.7$
Diffractive Selection	$x_{I\!P} < 0.03$ $M_Y < 1.6\ \mathrm{GeV}$ $\lvert t\rvert < 1\ \mathrm{GeV}^2$
Jet Selection	$p^{\star}_{T,jet1} > 5.5\ \mathrm{GeV}$ $p^{\star}_{T,jet2} > 4\ \mathrm{GeV}$ $-3 < \eta^{\star}_{jet} < 0$

Table 1: The kinematic domain in which the cross sections are measured at the level of jets of stable hadrons. The jets are reconstructed using the inclusive k_T algorithm as described in the text. Variables marked with a $\star$ are evaluated relative to the collision axis in the $\gamma^{\star}p$ centre of mass frame.

sets of parton densities, H1 2006 DPDF fit A and fit B, which differ in the parameterisation of the gluon density. A steeper fall-off in the gluon density at high $z_{I\!P}$ is obtained for fit B than for fit A, while the quark densities agree within the uncertainties. Both DPDF sets provide a good description of the inclusive diffractive DIS data.

The experimental and theoretical uncertainties on the DPDFs in [5] are propagated to the dijet prediction via an eigenvector decomposition of the error sources according to the method presented in [48]. The deviations from the nominal prediction are added in quadrature to obtain the uncertainty on the dijet prediction due to DPDF uncertainties. Alternative hadronisation corrections are extracted from the POMWIG Monte Carlo model [45], which uses cluster fragmentation [46, 47] to describe hadronisation. The difference between the nominal and alternative hadronisation corrections is taken to be the hadronisation uncertainty on the NLO QCD prediction. To account for the uncertainty due to the missing higher orders in the calculation, the renormalisation and factorisation scales are varied by common factors of 2 and 0.5 with respect to the nominal prediction.

3.5 Cross Section Measurement

The measured differential dijet cross sections are defined at the level of stable hadrons in the kinematic region specified in table 1. A correction of typically 20% is applied to account for detector acceptances, inefficiencies and migrations between measurement bins using the RAPGAP 3.1 Monte Carlo program. This simulation gives a reasonable description of the shapes of all data distributions. According to the simulation, the detector level observables are found to be well correlated with the observables at hadron level. The cross sections are corrected to the QED Born level using the HERACLES interface to the RAPGAP Monte Carlo program.

The small background contribution from non-diffractive deep-inelastic scattering is statistically subtracted using the Monte Carlo sample introduced above.

The cross section definition for this study is chosen to include all events with $M_Y < 1.6$ GeV and $|t| < 1$ GeV^2 as in [2, 5, 16–18]. As M_Y and $|t|$ are not measured directly, the effects of migration across these boundaries must be estimated. Migrations from large $M_Y > 5$ GeV and $x_{I\!P} > 0.2$ are corrected for using RAPGAP in inclusive mode. Smearing across the $M_Y = 1.6$ GeV boundary of events with $M_Y \leq 5$ GeV is evaluated with the DIFFVM [42] simulation of proton dissociation, following [2].

3.6 Systematic Uncertainties

The systematic uncertainties are evaluated separately for each measurement bin, except for uncertainties on global correction factors. The following sources of uncertainty are determined to be largely correlated between bins:

LAr calorimeter energy scale: The energy scale of the LAr calorimeter response to hadrons is varied by $\pm 4\%$ in the simulation, which causes a variation of the total cross section by $^{+5}_{-3}\%$ and slightly larger uncertainties in individual measurement bins.

Track Momenta: The contribution of the track momenta to the X system is varied by $\pm 3\%$, resulting in a total cross section uncertainty of around 3%.

Luminosity: The measurement of the integrated luminosity has an uncertainty of 1.5%. This translates directly into a 1.5% uncertainty on the cross section.

FMD noise: The cross section is corrected for the fraction of events rejected due to noise in the forward muon detector. A global correction factor is determined from a sample of randomly triggered events and is found to be $(1.2 \pm 0.4)\%$. The uncertainty on this correction factor leads to an overall normalisation uncertainty of 0.4%.

$x_{I\!P}$-migration: The estimated number of non-diffractive background events which migrate into the sample from the unmeasured region $x_{I\!P} > 0.03$ or $M_Y > 5$ GeV is varied by $\pm 50\%$, leading to a total cross section uncertainty of 1%.

M_Y and $|t|$ migrations: The systematic uncertainties connected to migrations over the M_Y and $|t|$ limits are assessed following the method of [5], giving a total uncertainty of 5%.

Rapidity gap selection inefficiency: A fraction of the events in the kinematic range specified in table 1 give rise to hadronic activity at pseudorapidities larger than allowed by the η_{max} cut in the LAr calorimeter or in the forward detectors and is thus lost. The correction for this effect relies heavily on the RAPGAP simulation to describe the forward energy flow of diffractive events. The forward energy flow in diffractive DIS is investigated with a sample of elastically scattered protons detected in the forward proton spectrometer of the H1 detector [49]. The study finds the RAPGAP model to describe these migrations to within 30% [50]. The effect of this uncertainty on this measurement is estimated by reweighting all events in the signal simulation which do not pass the forward detector cuts by $\pm 30\%$. This translates into an uncertainty of $^{+10}_{-5}\%$ on the total cross section.

The remaining systematic uncertainties, described below, show significantly less correlation and are thus treated as uncorrelated between measurement bins.

Positron energy: The energy of the scattered positron is known to within 2% at $E_e = 8$ GeV, falling linearly to 0.3% at $E_e = 27.5$ GeV. This translates into a 2% uncertainty on the total cross section.

Positron angle: The uncertainty in the polar angle θ_e of the scattered positron is 1 mrad. This contributes an uncertainty of 1% to the total cross section.

Trigger efficiency: The average difference between the trigger efficiency as extracted from the Monte Carlo simulation and from the data using monitor trigger samples is taken as the uncertainty on the trigger efficiency, which is around 1%.

Unfolding uncertainties: To evaluate the model dependence of the correction from the detector to the hadron level, key kinematic dependences of the Monte Carlo simulation are reweighted within the limits imposed by the present data. The following distributions are varied: $x_{I\!P}$ by $x_{I\!P}^{\pm 0.2}$, $\hat{p}_T$ by $\hat{p}_T^{\pm 0.4}$, $|t|$ by $e^{\pm 2t\ \mathrm{GeV}^{-2}}$ and y by $y^{\pm 0.3}$. The largest uncertainty is introduced by the $\hat{p}_T$ reweighting (typically 4%) followed by $x_{I\!P}$ (3%), while the reweights in the two other variables have rather small effects.

The largest contributions to the systematic errors on the cross sections arise from the uncertainty in the LAr calorimeter energy scale, from unfolding uncertainties and from the rapidity gap selection inefficiency. The overall uncertainty on the total cross section is $^{+15}_{-10}\%$. The uncertainties on individual measurement bins are slightly larger.

4 Dijet Results

The integrated cross section in the kinematic range specified in table 1 is determined to be

$$\sigma^{2jets}(ep \to eXY) = 52 \pm 1\ (\mathrm{stat.})\ ^{+7}_{-5}\ (\mathrm{syst.})\ \mathrm{pb}.$$

When this measurement is translated to the kinematic range of the previous H1 result [18] (i.e. after correcting for the different proton beam energies, y-range and $p^{\star}_{T,jet1}$-ranges), the two results are compatible within the uncertainties. The total cross section can be compared to the NLO QCD predictions based on the two sets of DPDFs determined from inclusive diffraction [5]:

$$\sigma^{2jets}(\mathrm{H1\ 2006\ DPDF\ fit\ A}) = 75\ ^{+27}_{-17}\ (\mathrm{scale\ unc.})\ \pm 7(\mathrm{DPDF})\ \mathrm{pb},$$
$$\sigma^{2jets}(\mathrm{H1\ 2006\ DPDF\ fit\ B}) = 57\ ^{+21}_{-13}\ (\mathrm{scale\ unc.})\ \pm 8(\mathrm{DPDF})\ \mathrm{pb}.$$

The scale uncertainty is derived by simultaneously varying μ_f and μ_r by common factors of 2 and 0.5. Whilst both predictions are compatible with the measurement, the central result of fit A overestimates the cross section by $\sim 40\%$.

Differential dijet cross sections are shown in figures 2 to 6 and tabulated in tables 4 to 10. Cross sections as a function of y, $x_{I\!P}$, $p^{\star}_{T,jet1}$ and $\Delta\eta^{\star}_{jets} = |\eta^{\star}_{jet1} - \eta^{\star}_{jet2}|$ are shown in Figure 2 and are compared to NLO QCD predictions. Differential cross sections as a function of $z_{I\!P}$ are shown in Figure 3. The NLO QCD prediction for the highest bin in $z_{I\!P}$ is not shown due to problems in evaluating the hadronisation corrections[1].

The prediction based on H1 2006 DPDF fit B describes the shapes of all distributions well, whereas some discrepancies are apparent between the fit A and the data. The largest differences between the shapes of the two predictions can be seen in $z_{I\!P}$ and y, which are correlated through the kinematics. The discrepancies between Fit A and the data are most prominent in the region of high $z_{I\!P}$ ($z_{I\!P} \gtrsim 0.4$), where the prediction is clearly too high. The good agreement in the $x_{I\!P}$ distribution between the dijet data and the predictions indicates that the pomeron flux (which governs this distribution) for jet production does not differ significantly from the flux describing inclusive diffraction. The shapes of the $\Delta\eta^{\star}_{jets}$ and $p^{\star}_{T,jet1}$ distributions are determined by the hard scattering matrix elements and are rather insensitive to the DPDFs. The agreement in these distributions shows that the NLO QCD computation, which uses boson gluon fusion as the dominant process, is adequate to describe dijet production in this kinematic regime.

The large difference between the two predictions at high $z_{I\!P}$ reflects the large uncertainty on the gluon density in this range as determined from inclusive data alone. Figure 3 also indicates the sensitivity of the dijet data to the gluon density at large $z_{I\!P}$. To test factorisation in a region where the gluon density is well determined from the inclusive data, the dijet cross section is also measured in the reduced kinematic domain of $z_{I\!P} < 0.4$. The results are shown in Figure 4 and are compared with predictions based on the H1 2006 DPDF fits. In this kinematic region both fits agree well with the dijet data, supporting the notion of QCD factorisation within uncertainties.

5 Combined NLO QCD Fit

A NLO QCD fit is used to determine the diffractive quark singlet and gluon densities. This combined fit uses both the measurements of the diffractive dijet cross sections presented in this paper and the measurement of the inclusive diffractive cross section presented in [5]. The combined fit shall henceforth be referred to as 'H1 2007 Jets DPDF'.

5.1 Data Sets

Assuming the factorisation hypothesis, the differential dijet cross section as a function of $z_{I\!P}$ is used in the fit in four bins of $Q^2+p^{\star 2}_{T,jet1}$, which is taken to be the scale variable. These measured cross sections are shown in figure 5 and tables 9 and 10 for dijets at the stable hadron level in the kinematic range specified in table 1. The fit also includes the measurements of inclusive diffraction obtained by H1 in [5], which are presented in the form of the reduced diffractive deep-inelastic scattering cross section $\sigma_r^{D(3)}$, defined through

[1]In some cases the Lund string fragmentation algorithm turns the entire system X into just two mesons. This leads to events having $z_{I\!P} \simeq 1$ at the hadron level independently of their parton level $z_{I\!P}$ and to corresponding migration problems.

$$\frac{d^3\sigma_{ep\to eXY}}{dx_{I\!P}d\beta dQ^2} = \frac{4\pi\alpha_{em}^2}{\beta^2 Q^4} \cdot Y_+ \cdot \sigma_r^{D(3)}(x_{I\!P}, \beta, Q^2),$$

where $Y_+ = 1 + (1-y)^2$. In leading order the reduced cross section $\sigma_r^{D(3)}$ is identical to $F_2^{D(3)}$. The small influence of the longitudinal structure function $F_L^{D(3)}$ is included here via its NLO dependence on the DPDFs. Following the treatment in [5] only data in the range $Q^2 \geq 8.5\ \mathrm{GeV}^2$, $M_X \geq 2\ \mathrm{GeV}$ and $\beta \leq 0.8$ are included in the fit. Figures 7 and 8 show the inclusive data points in the form of the product $x_{I\!P} \cdot \sigma_r^{D(3)}(x_{I\!P}, \beta, Q^2)$.

5.2 Fit Ansatz

The DPDFs $f_i^D(z, \mu_f^2, x_{I\!P}, t)$ are parameterised following the fit procedure of the inclusive analysis [5]. They are factorised into a pomeron flux $f_{I\!P/p}(x_{I\!P}, t)$ and parton densities of the pomeron $f_i(z, \mu_f^2)$ using the proton vertex factorisation ansatz

$$f_i^D(z, \mu_f^2, x_{I\!P}, t) = f_{I\!P/p}(x_{I\!P}, t) \cdot f_i(z, \mu_f^2).$$

The parton densities f_i are modelled as a singlet distribution $\Sigma(z, \mu_f^2)$ consisting of the three light quark and corresponding antiquark distributions, which are all assumed to be of equal magnitude, and a gluon distribution $g(z, \mu_f^2)$. Here z is the longitudinal momentum fraction of the parton entering the hard subprocess with respect to the diffractive exchange, such that $z = \beta = x/x_{I\!P}$ and $z = z_{I\!P}$ for the lowest order quark parton model process in inclusive diffraction and for dijets, respectively. The parton densities $f_i(z, \mu_f^2)$ are parameterised at a starting scale of $\mu_{f,0}^2 = 2.5\ \mathrm{GeV}^2$ and are evolved to higher factorisation scales using a numerical solution of the NLO DGLAP evolution equations. The singlet and gluon distributions are parameterised at the starting scale as

$$f_i(z, \mu_{f,0}^2) \equiv A_i \cdot z^{B_i} \cdot (1-z)^{C_i}.$$

The parameterisation of the singlet density is thus identical to that used in the analysis of inclusive diffraction [5]. The parameterisation of the gluon density differs in that the H1 2006 DPDF fit A omits the factor $z^{B_{gluon}}$, while fit B omits both $z^{B_{gluon}}$ and $(1-z)^{C_{gluon}}$. In the H1 2007 Jets DPDF fit, where the dijet data additionally constrain the gluon, the χ^2 of the fit is significantly reduced by the inclusion of the factor $z^{B_{gluon}}$.

The pomeron flux is parameterised as in [5] using a form motivated by Regge theory:

$$f_{I\!P/p}(x_{I\!P}, t) = A_{I\!P} \left(\frac{1}{x_{I\!P}}\right)^{2\alpha_{I\!P}(t)-1} e^{B_{I\!P}t}.$$

The normalisation parameter $A_{I\!P}$ is defined as in [5]. The pomeron trajectory $\alpha_{I\!P}(t)$ is assumed to be linear:

$$\alpha_{I\!P}(t) = \alpha_{I\!P}(0) + \alpha'_{I\!P} \cdot t.$$

Parameter	Value		Source
$\alpha'_{I\!P}$	$0.06^{+0.19}_{-0.06}$	GeV^{-2}	[52]
$B_{I\!P}$	$5.5^{+0.7}_{-2.0}$	GeV^{-2}	[52]
$\alpha_{I\!R}(0)$	0.5 ± 0.1		[2]
$\alpha'_{I\!R}$	$0.3^{+0.6}_{-0.3}$	GeV^{-2}	[52]
$B_{I\!R}$	$1.6^{+0.4}_{-1.6}$	GeV^{-2}	[52]
m_c	1.4 ± 0.2	GeV	[53]
m_b	4.5 ± 0.5	GeV	[53]
$\alpha_s(M_Z^2)$	0.118 ± 0.002		[53]

Table 2: Fixed parameters and associated uncertainties used in the H1 2007 Jets DPDF.

For comparison with the data, all DPDFs are integrated over the measured range $|t| < 1\ \mathrm{GeV}^2$. To properly describe the data, especially at high $x_{I\!P}$, it is necessary to include a sub-leading exchange (the so called reggeon, $I\!R$, for details see [5]). This contribution is assumed to factorise similarly to the pomeron, so that the definition of the diffractive parton densities is modified to

$$f_i^D(z,\mu_f^2,x_{I\!P},t) = f_{I\!P/p}(x_{I\!P},t)\cdot f_i(z,\mu_f^2) + n_{I\!R}\cdot f_{I\!R/p}(x_{I\!P},t)\cdot f_i^{I\!R}(z,\mu_f^2).$$

The reggeon flux $f_{I\!R/p}(x_{I\!P},t)$ is parameterised in the same way as the pomeron flux. The parton densities $f_i^{I\!R}(z,Q^2)$ are taken from a parameterisation of pion structure function data [51]. The free parameters of the fit are the six parameters of the initial parton densities, $\alpha_{I\!P}(0)$ and the normalisation of the reggeon flux $n_{I\!R}$. All other parameters are fixed using the same values and uncertainties as in [5] as listed in table 2.

5.3 Fit Procedure

The fit is performed by minimisation of a χ^2 function, defined similarly to that in [5]. At each step of the minimisation procedure, the predictions for $\sigma_r^{D(3)}$ are calculated at NLO in the $\overline{MS}$ renormalisation scheme with the QCDFIT program [54,55]. For the prediction of the dijet cross section the combined fit uses the 'matrix method' introduced by the ZEUS collaboration [56], together with the NLOJET++ program. This procedure has been shown to yield results which agree with direct NLOJET++ predictions in the selected fit range to better than 2% after one iteration of the input DPDFs (for details see [57]). Whereas the NLOJET++ calculation employs a massless heavy flavour scheme, the prediction for σ_r^D is performed with massive charm and beauty quarks. However, for the dijet data the hard scale is typically much larger than the charm mass ($\mu_{r,f}^2 > 29\ \mathrm{GeV}^2 \gg m_c^2$), so little effect is expected. This is confirmed by performing fits to the inclusive data alone in both schemes, resulting in very similar gluon densities in the Q^2 range to which the dijets are sensitive.

The inclusive and dijet data sets are statistically independent and the correlations between the two measurements through the systematic uncertainties are small. The χ^2 function treats the combined statistical und uncorrelated systematic errors for each data point in the usual way and also takes account of correlated uncertainties within the inclusive or dijet data sets by allowing variations in the corresponding systematic error sources at the expense of increases in the χ^2 variable [58]. As in [5], there are ten such error sources for inclusive data. The correlated errors on the jet cross sections are treated via a single additional parameter in the χ^2 finction

Besides the uncertainties related to the cross section measurements, the extracted DPDFs are affected by uncertainties in the fit procedure and its theory input. The fit errors include the rather small effects of the uncertainties on the input parameters as given in table 2. The uncertainty in the relative scale choice between the inclusive and dijet data is estimated by varying the scale for the dijet data between $2 \cdot \sqrt{Q^2 + p^{\star 2}_{T,jet1}}$ and $0.5 \cdot \sqrt{Q^2 + p^{\star 2}_{T,jet1}}$ whilst keeping Q as the scale for the inclusive data. In addition the effects of changing the fit range in $z_{I\!P}$ (excluding dijet events with $z_{I\!P} < 0.2$) or the starting scale $\mu^2_{f,0}$ (using $3.5\ \mathrm{GeV}^2$ instead of $2.5\ \mathrm{GeV}^2$) are evaluated and included in the presented uncertainties. To assess the dependence of the final fitted parton densities on the hadronisation correction applied to the dijets, alternative correction factors extracted from the POMWIG Monte Carlo model are used. The deviation from the nominal fit result is included in the theoretical parton density uncertainties. The largest theoretical error contribution to the fitted gluon density at high $z_{I\!P}$ comes from the uncertainty in the relative scale of the two data sets.

6 H1 2007 Jets DPDF Fit Results

The fit results for the free parameters are summarized in table 3. The fit describes the data well as indicated by the overall value of χ^2/ndf = 196/218, which splits into χ^2 = 27 for the 36 dijet data points and χ^2 = 169 for the 190 $\sigma_r^{D(3)}$ data points. Thus the partial χ^2 for the inclusive data is slightly larger in the combined fit than in the fits to $\sigma_r^{D(3)}$ from [5], where χ^2 = 158 (164) for the H1 2006 DPDF fit A (B), indicating a small remaining tension between the two data sets. The parameter C_{gluon}, determining the gluon density behaviour at high values of z, is positive in the combined fit in accordance with the expectation that the gluon density should not be singular for $z \to 1$. This behaviour is different from the H1 DPDF fit A, where C_{gluon} is determined to be negative and the gluon density is artificially suppressed at very high z using an additional exponential factor.

The dijet cross sections are well described by the predictions based on the H1 2007 Jets DPDF as shown in figures 5 and 6. Figures 7 and 8 show the measurements of $\sigma_r^{D(3)}$ as a function of Q^2 for different values of β and $x_{I\!P}$, together with the NLO predictions based on the H1 2007 Jets DPDF fit. The results of fits A and B to the inclusive data alone are also shown. A very good description is obtained with all three fits.

The diffractive gluon distribution and the quark singlet distribution are shown in figure 9 for scales of $\mu_f^2 = 25\ \mathrm{GeV}^2$ and $\mu_f^2 = 90\ \mathrm{GeV}^2$, together with the results of fits A and B of the stand-alone analysis of $\sigma_r^{D(3)}$. The error bands indicate the uncertainties due to experimental sources and the theoretical errors inherent in the fit procedure. The uncertainties on the quark distribution and on the gluon distribution at low $z_{I\!P}$ are dominated by the experimental uncertainties, while the uncertainty on the gluon density at high $z_{I\!P}$ recieves sizeable contributions from both experimental and theoretical sources.

Parameter	Fit Value (H1 2007 Jets DPDF)
$\alpha_{I\!P}(0)$	1.104 ±0.007
$n_{I\!R}$	$1.3\times10^{-3}\pm0.4\times10^{-3}$
A_{gluon}	0.88 ±0.17
B_{gluon}	0.33 ±0.10
C_{gluon}	0.91 ±0.18
A_{quark}	0.13 ±0.02
B_{quark}	1.5 ±0.12
C_{quark}	0.51 ±0.08
χ^2/ndf	196/218

Table 3: H1 2007 Jets DPDF fit parameters obtained from the combined fit to the diffractive inclusive and dijet data. Only the experimental uncertainties are given.

The combined fit constrains both the diffractive gluon and quark densities well and for the first time with comparable precision in the complete range $0.05 < z_{I\!P} < 0.9$. At high $z_{I\!P}$ the resulting gluon density differs significantly from that of H1 2006 DPDF fit A, but is compatible with fit B [5]. Good agreement is seen between all three fits for the singlet quark density and the gluon density at low $z_{I\!P}$. The values of $\alpha_{I\!P}(0) = 1.104 \pm 0.007$ and $n_{I\!R} = (1.3 \pm 0.4) \times 10^{-3}$ are compatible within experimental uncertainties with the value extracted in H1 2006 fit B. The uncertainties on these parameters are not significantly decreased by the inclusion of the dijet data compared to the determination from the inclusive data alone.

In figure 10 the DPDFs as determined by H1 are compared with the results of an independent analysis [15], where parton densities are derived from the same inclusive diffractive data [5]. A hybrid theoretical framework is used which combines aspects of collinear factorisation and a perturbative two-gluon-exchange model [59–62]. Most of the dijets events are produced via BGF-type processes as in figure 1. At high β, there is an additional contribution in which the perturbative two-gluon state participates directly in the hard interaction via photon-pomeron fusion, leading to a modified evolution equation for the DPDFs. The resulting DPDFs agree reasonably well with the H1 2007 Jets DPDF and with the H1 2006 DPDF fit B.

Measurements of diffractive charm production by H1 have also been compared to predictions based on the DPDFs presented in this paper [63]. Whilst overall good agreement is obtained, the statistical accuracy of the charm measurement limits its power to discriminate between different DPDF sets.

7 Conclusion

Cross sections for dijet production in diffractive deep-inelastic scattering are measured with improved precision compared to earlier analyses. Single and double differential cross sections are presented in a variety of variables sensitive to the underlying dynamics of hard diffraction. NLO QCD predictions based on diffractive parton densities extracted from measurements of inclusive diffractive deep-inelastic scattering describe the data well in the kinematic region where the gluon density is reliably constrained by the inclusive measurements. This agreement confirms the validity of QCD factorisation and thus the applicability of diffractive parton densities evolving according to the DGLAP equations.

A combined fit to diffractive inclusive and dijet data is performed, using NLO QCD calculations based on QCD factorisation and DGLAP evolution. Both data sets are described well by the fit. The inclusion of the dijet data allows the simultaneous determination of both the diffractive gluon and the singlet quark distribution with good and comparable accuracy in the range $0.05 < z_{I\!P} < 0.9$. This is the first reliable determination of the diffractive gluon density up to large momentum fractions.

Acknowledgments

We are grateful to the HERA machine group whose outstanding efforts have made this experiment possible. We thank the engineers and technicians for their work in constructing and maintaining the H1 detector, our funding agencies for financial support, the DESY technical staff for continual assistance, and the DESY directorate for the support and the hospitality which they extend to the non DESY members of the collaboration.

References

[1] J. C. Collins, Phys. Rev. D **57** (1998) 3051 [Erratum-ibid. D **61** (2000) 019902] [hep-ph/9709499].

[2] C. Adloff *et al.* [H1 Collaboration], Z. Phys. C **76** (1997) 613 [hep-ex/9708016].

[3] A. D. Martin, M. G. Ryskin and G. Watt, Eur. Phys. J. C **37** (2004) 285 [hep-ph/0406224].

[4] A. D. Martin, M. G. Ryskin and G. Watt, Eur. Phys. J. C **44** (2005) 69 [hep-ph/0504132].

[5] A. Aktas *et al.* [H1 Collaboration], Eur. Phys. J. C **48** (2006) 715 [hep-ex/0606004].

[6] S. Chekanov *et al.* [ZEUS Collaboration], Eur. Phys. J. C **38** (2004) 43 [hep-ex/0408009].

[7] F. Hautmann, Z. Kunszt and D. E. Soper, Nucl. Phys. B **563** (1999) 153 [hep-ph/9906284].

[8] F. Hautmann and D. E. Soper, Phys. Rev. D **63** (2001) 011501 [hep-ph/0008224].

[9] J. Breitweg *et al.* [ZEUS Collaboration], Eur. Phys. J. C **5** (1998) 41 [hep-ex/9804013].

[10] K. Golec-Biernat and J. Kwiecinski, Phys. Lett. B **353** (1995) 329 [hep-ph/9504230].

[11] T. Gehrmann and W. J. Stirling, Z. Phys. C **70** (1996) 89 [hep-ph/9503351].

[12] L. Alvero, J. C. Collins, J. Terron and J. J. Whitmore, Phys. Rev. D **59** (1999) 074022 [hep-ph/9805268].

[13] C. Royon, L. Schoeffel, J. Bartels, H. Jung and R. Peschanski, Phys. Rev. D **63** (2001) 074004 [hep-ph/0010015].

[14] G. Watt, published in “Ringberg 2005, New trends in HERA physics” 303 [hep-ph/0511333].

[15] A. D. Martin, M. G. Ryskin and G. Watt, Phys. Lett. B **644** (2007) 131 [hep-ph/0609273].

[16] C. Adloff *et al.* [H1 Collaboration], Eur. Phys. J. C **6** (1999) 421 [hep-ex/9808013].

[17] C. Adloff *et al.* [H1 Collaboration], Eur. Phys. J. C **20** (2001) 29 [hep-ex/0012051].

[18] A. Aktas *et al.* [H1 Collaboration], accepted by Eur. Phys. J. C [hep-ex/0703022].

[19] C. Adloff *et al.* [H1 Collaboration], Phys. Lett. B **520** (2001) 191 [hep-ex/0108047].

[20] A. Aktas *et al.* [H1 Collaboration], Eur. Phys. J. C **50** (2007) 1 [hep-ex/0610076].

[21] S. Chekanov *et al.* [ZEUS Collaboration], Nucl. Phys. B **672** (2003) 3 [hep-ex/0307068].

[22] S. Chekanov *et al.* [ZEUS Collaboration], Phys. Lett. B **545** (2002) 244 [hep-ex/0206020].

[23] S. Chekanov *et al.* [ZEUS Collaboration], Phys. Lett. B **516** (2001) 273 [hep-ex/0107004].

[24] V. A. Khoze, A. D. Martin and M. G. Ryskin, "Insight into double-pomeron-exchange Higgs production and backgrounds," [hep-ph/0702213].

[25] S. D. Ellis and D. E. Soper, Phys. Rev. D **48** (1993) 3160 [hep-ph/9305266].

[26] I. Abt *et al.* [H1 Collaboration], Nucl. Instrum. Meth. A **386** (1997) 310.

[27] I. Abt *et al.* [H1 Collaboration], Nucl. Instrum. Meth. A **386** (1997) 348.

[28] R. D. Appuhn *et al.* [H1 SPACAL Group], Nucl. Instrum. Meth. A **386** (1997) 397.

[29] D. Pitzl *et al.*, Nucl. Instrum. Meth. A **454** (2000) 334 [hep-ex/0002044].

[30] B. Andrieu *et al.* [H1 Calorimeter Group], Nucl. Instrum. Meth. A **336** (1993) 460.

[31] B. Andrieu *et al.* [H1 Calorimeter Group], Nucl. Instrum. Meth. A **336** (1993) 499.

[32] C. Adloff *et al.* [H1 Collaboration], Z. Phys. C **74** (1997) 221 [hep-ex/9702003].

[33] R. Brun *et al.*, "GEANT 3 User's Guide", 1987, `CERN-DD/EE/84-1`.

[34] H. Jung, Comput. Phys. Commun. **86** (1995) 147; version 3.10 is used.

[35] F. P. Schilling [H1 Collaboration], Acta Phys. Polon. B **33** (2002) 3419 [hep-ex/0209001].

[36] M. Bengtsson and T. Sjöstrand, Z. Phys. C **37** (1988) 465.

[37] T. Sjöstrand, Comput. Phys. Commun. **39** (1986) 347.

[38] T. Sjöstrand and M. Bengtsson, Comput. Phys. Commun. **43** (1987) 367.

[39] A. Kwiatkowski, H. Spiesberger and H. J. Mohring, Comput. Phys. Commun. **69** (1992) 155.

[40] G. A. Schuler and T. Sjöstrand, Phys. Lett. B **376** (1996) 193 [hep-ph/9601282].

[41] H. L. Lai *et al.* [CTEQ Collaboration], Eur. Phys. J. C **12** (2000) 375 [hep-ph/9903282].

[42] B. List, A. Mastroberardino, "DIFFVM: A Monte Carlo Generator for diffractive processes in ep scattering" in A. Doyle *et al.* (eds.), Proc. of the Workshop on Monte Carlo Generators for HERA Physics, DESY-PROC-1999-02 (1999) 396.

[43] B. List, "Diffraktive J/ψ Produktion in Elektron - Proton Stößen am Speicherring HERA", Technische Universität Berlin, Diploma Thesis (1993).

[44] Z. Nagy and Z. Trocsanyi, Phys. Rev. Lett. **87** (2001) 082001 [hep-ph/0104315].

[45] B. E. Cox and J. R. Forshaw, Comput. Phys. Commun. **144** (2002) 104 [hep-ph/0010303].

[46] G. Marchesini and B. R. Webber, Nucl. Phys. B **310** (1988) 461.

[47] B. R. Webber, Nucl. Phys. B **238** (1984) 492.

[48] W. Giele *et al.*, published in "Les Houches 2001, Physics at TeV colliders" 275, chapter 1, [hep-ph/0204316].

[49] P. Van Esch *et al.*, Nucl. Instrum. Meth. A **446** (2000) 409 [hep-ex/0001046].

[50] S. Schenk, "Energy Flow in Hard Diffractive Deep-Inelastic Scattering and Photopro duction with a Leading Proton", Universität Heidelberg, Diploma Thesis (2003).

[51] A. D. Martin, R. G. Roberts, W. J. Stirling and R. S. Thorne, Eur. Phys. J. C **28** (2003) 455 [hep-ph/0211080].

[52] A. Aktas *et al.* [H1 Collaboration], Eur. Phys. J. C **48** (2006) 749 [hep-ex/0606003].

[53] S. Eidelman *et al.* [Particle Data Group], Phys. Lett. B **592** (2004) 1.

[54] M. Botje, M. Klein and C. Pascaud, published in "Hamburg 1995/96, Future physics at HERA" 33-51, [hep-ph/9609489].

[55] C. Pascaud and F. Zomer, "QCD Analysis From The Proton Structure Function F2 Measurement: Issues On Fitting, Statistical And Systematic Errors," LAL-95-05.

[56] S. Chekanov *et al.* [ZEUS Collaboration], Eur. Phys. J. C **42** (2005) 1 [hep-ph/0503274].

[57] M. U. Mozer, "Measurement and QCD analysis of diffractive jet cross sections in deep-inelastic scattering at HERA", Universität Heidelberg, PhD Thesis (2006), available from http://www-h1.desy.de/publications/theses_list.html.

[58] C. Adloff *et al.* [H1 Collaboration], Eur. Phys. J. C **21** (2001) 33 [hep-ex/0012053].

[59] J. Bartels, H. Lotter and M. Wüsthoff, Phys. Lett. B **379** (1996) 239 [Erratum-ibid. B **382** (1996) 449] [hep-ph/9602363].

[60] J. Bartels, C. Ewerz, H. Lotter and M. Wüsthoff, Phys. Lett. B **386** (1996) 389 [hep-ph/9605356].

[61] J. Bartels, H. Jung and M. Wüsthoff, Eur. Phys. J. C **11** (1999) 111 [hep-ph/9903265].

[62] J. Bartels, H. Jung and A. Kyrieleis, Eur. Phys. J. C **24** (2002) 555 [hep-ph/0204269].

[63] M. Kapichine, "Diffractive Final States: Dijets and Charm ," to appear in the Proceedings of the 33rd International Conference On High Energy Physics, July 2006, Moscow.

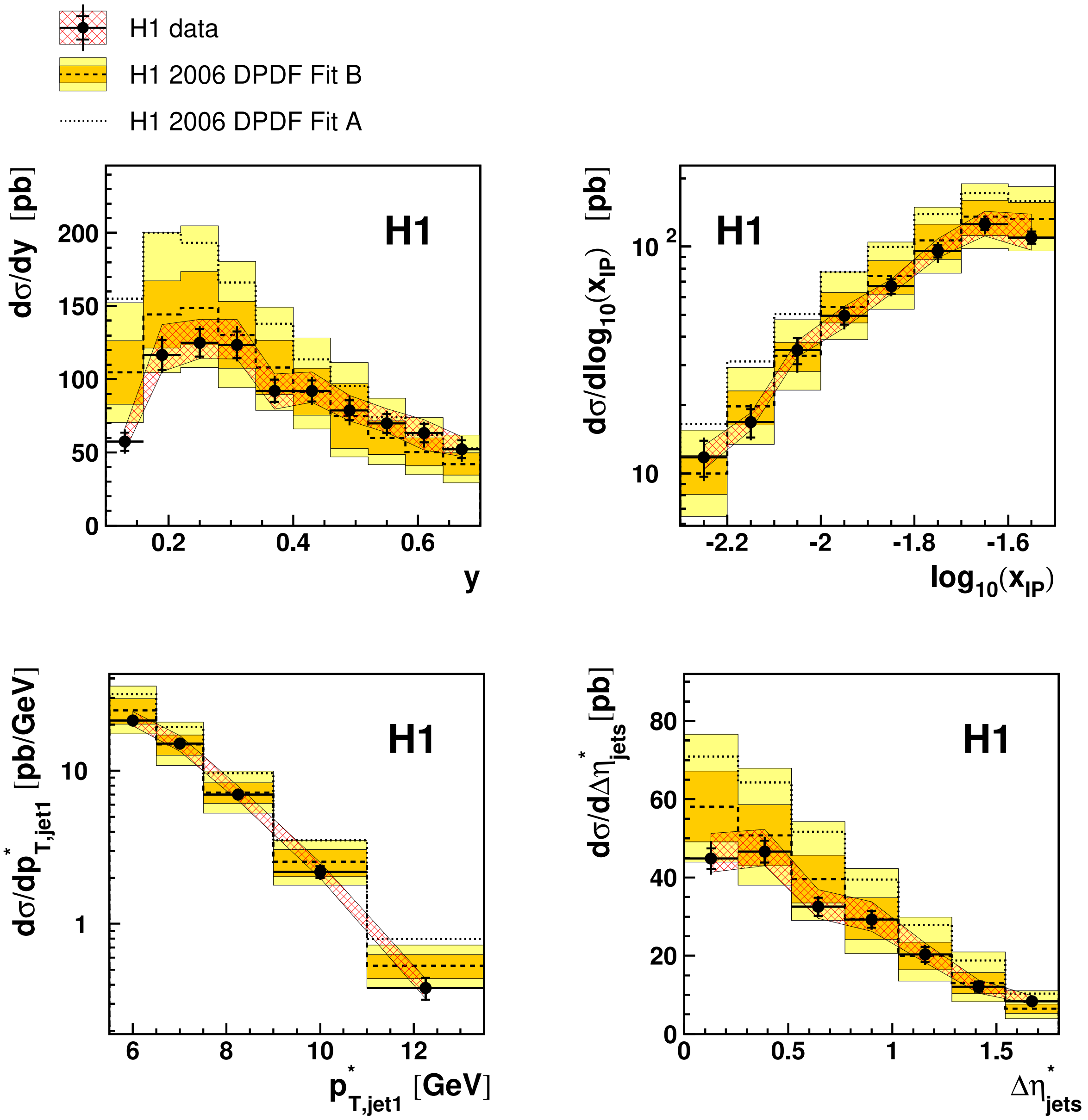

Figure 2: Cross sections for diffractive dijets, differential in y, $\log x_{I\!P}$, $p^{\star}_{T,jet1}$ and $\Delta\eta^{\star}_{jets}$ compared to NLO predictions based on the parton-densities from the H1 2006 DPDF fits [5]. The data are shown as black points with the inner and outer error bars denoting the statistical and quadratically added uncorrelated systematic uncertainties, respectively. The hatched band indicates the correlated systematic uncertainty. The dashed line shows the NLO QCD prediction based on the H1 2006 DPDF fit B, which is surrounded by a dark shaded band indicating the parton density and hadronisation uncertainties. In the light shaded band the scale uncertainty is added quadratically to the parton density and hadronisation uncertainties. The dotted line represents the NLO QCD prediction based on the H1 2006 DPDF fit A.

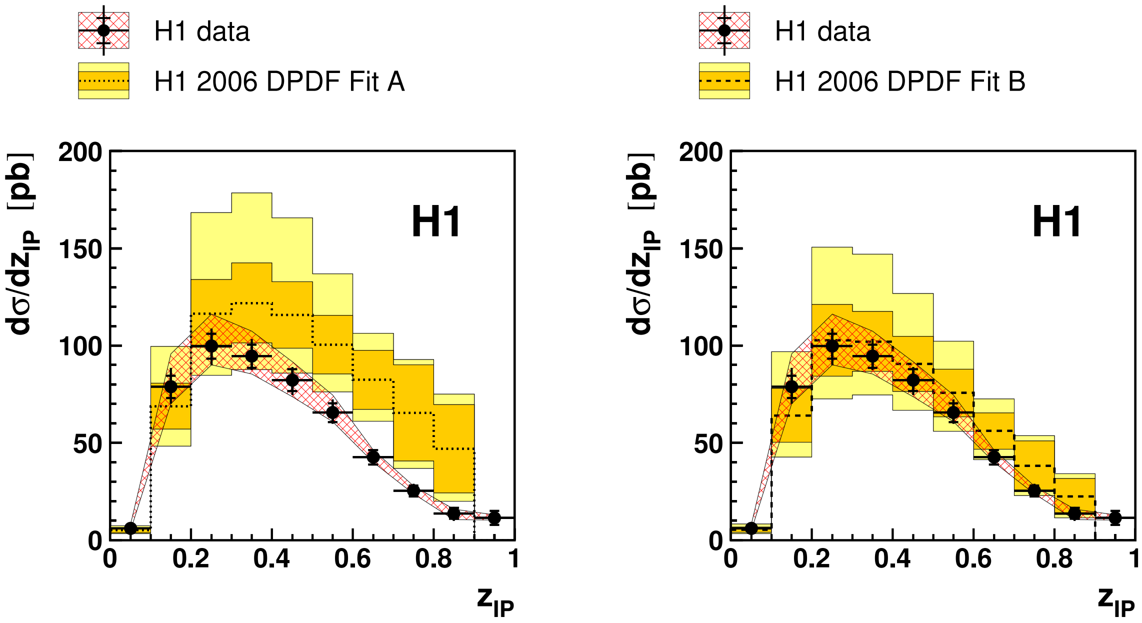

Figure 3: Cross section for diffractive dijets, differential in $z_{I\!P}$ compared to NLO predictions based on the parton-densities from the H1 2006 DPDF fits [5]. The data are shown as black points with the inner and outer error bars denoting the statistical and quadratically added uncorrelated systematic uncertainties, respectively. The hatched band indicates the correlated systematic uncertainty. In the left panel the data are compared to the NLO QCD prediction based on the H1 2006 DPDF fit A (dotted line) and in the right panerl to the prediction based on the H1 2006 DPDF fit B (dashed line). The lines are surrounded by a dark shaded band indicating the parton density and hadronisation uncertainties. In the light shaded band the scale uncertainty is added quadratically to the parton density and hadronisation uncertainties. The prediction for $z_{I\!P} > 0.9$ is not shown since the hadronisation corrections for this bin cannot be determined reliably.

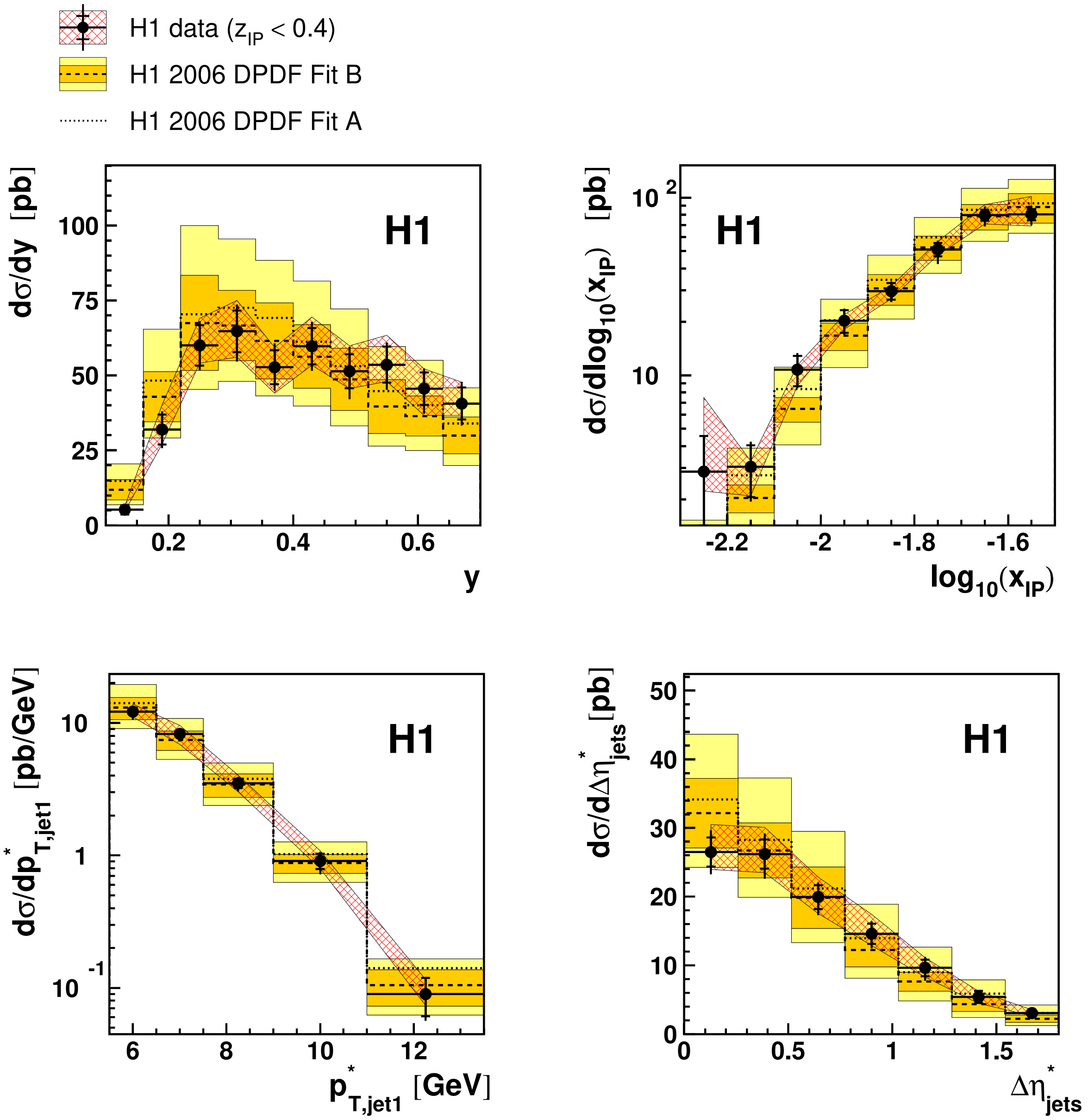

Figure 4: Cross sections for diffractive dijets restricted to $z_{I\!P} < 0.4$, differential in y, $\log x_{I\!P}$, $p^{\star}_{T,jet1}$ and $\Delta\eta^{\star}_{jets}$ compared to NLO predictions based on the parton-densities from the H1 2006 DPDF fits [5]. The data are shown as black points with the inner and outer error bars denoting the statistical and quadratically added uncorrelated systematic uncertainties, respectively. The hatched band indicates the correlated systematic uncertainty. The dashed line shows the NLO QCD prediction based on the H1 2006 DPDF fit B, which is surrounded by a dark shaded band indicating the parton density and hadronisation uncertainties. In the light shaded band the scale uncertainty is added quadratically to the parton density and hadronisation uncertainties. The dotted line represents the NLO QCD prediction based on the H1 2006 DPDF fit A.

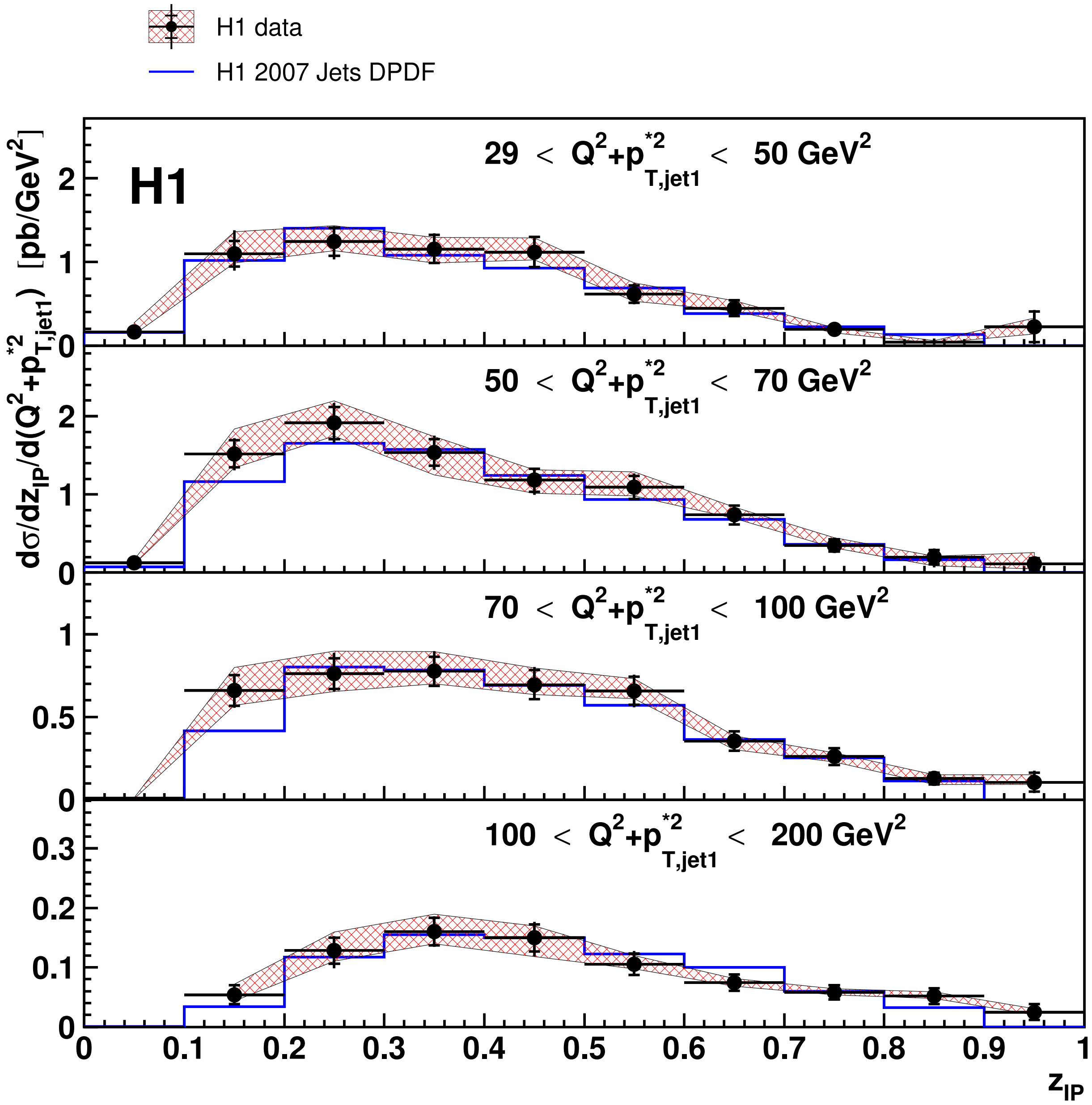

Figure 5: Cross section for diffractive dijet production doubly differential in $z_{I\!P}$ and the scale $Q^2 + p^{\star 2}_{T,jet1}$. The data are shown as black points with the inner and outer error bars denoting the statistical and quadratically added uncorrelated systematic uncertainties, respectively. The hatched band indicates the correlated systematic uncertainty. The solid line shows the NLO QCD prediction based on the H1 2007 Jets DPDF. Data points in the highest $z_{I\!P}$ bin were not included in the fit since the hadronisation corrections cannot be evaluated reliably.

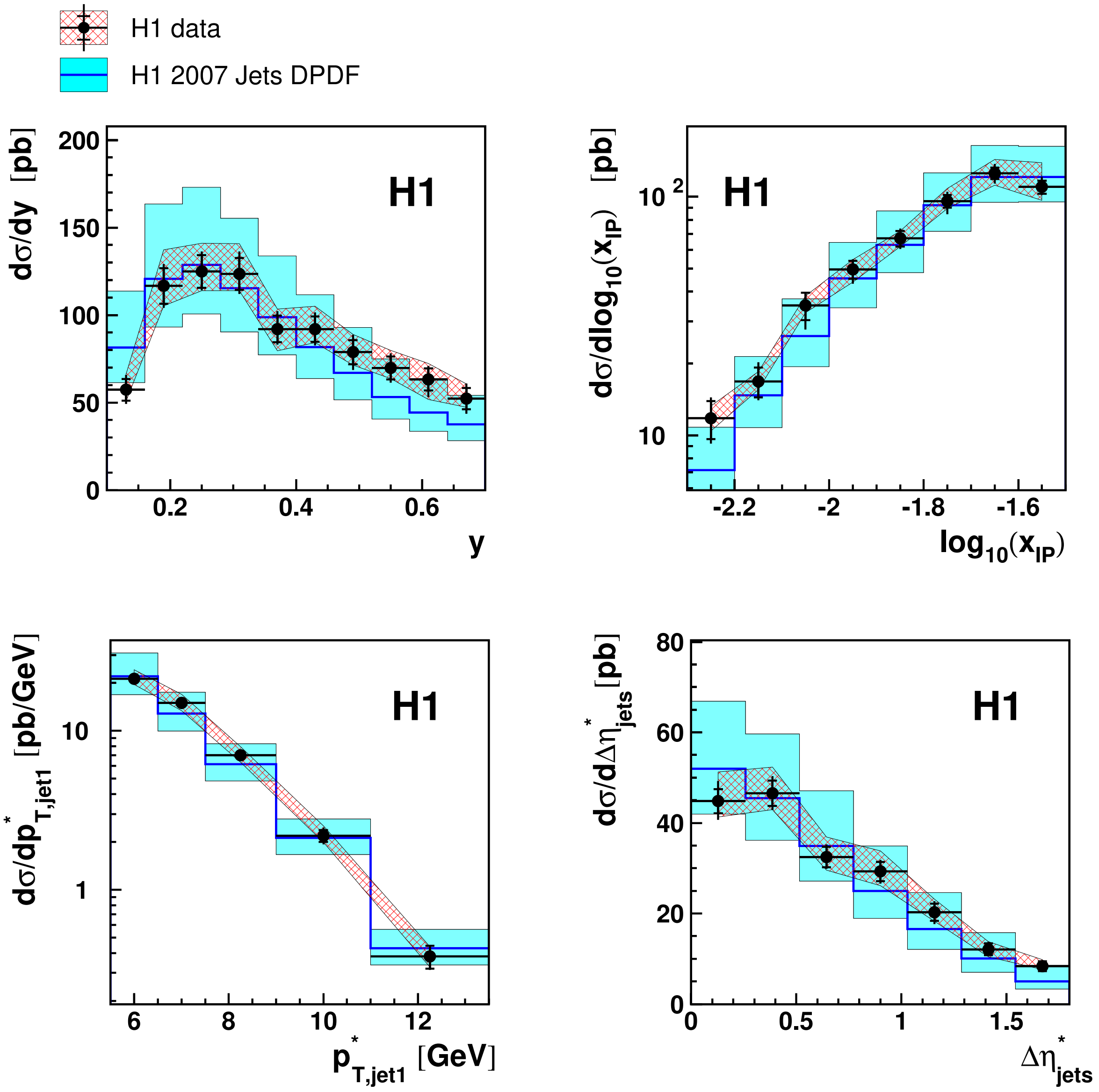

Figure 6: Cross sections for diffractive dijet production differential in the variables y, $\log x_{I\!P}$, $p^{\star}_{T,jet1}$ and $\Delta\eta^{\star}_{jets}$. The data are shown as black points with the inner and outer error bars denoting the statistical and quadratically added uncorrelated systematic uncertainties, respectively. The hatched band indicates the correlated systematic uncertainty. The solid line surrounded by the shaded band shows the NLO QCD prediction based on the H1 2007 Jets DPDF, where the band denotes the scale uncertainty derived by varying the renormalisation and factorisation scale $\mu = \sqrt{Q^2 + p^2_{T,jet1}}$ by factors of 2 and 0.5.

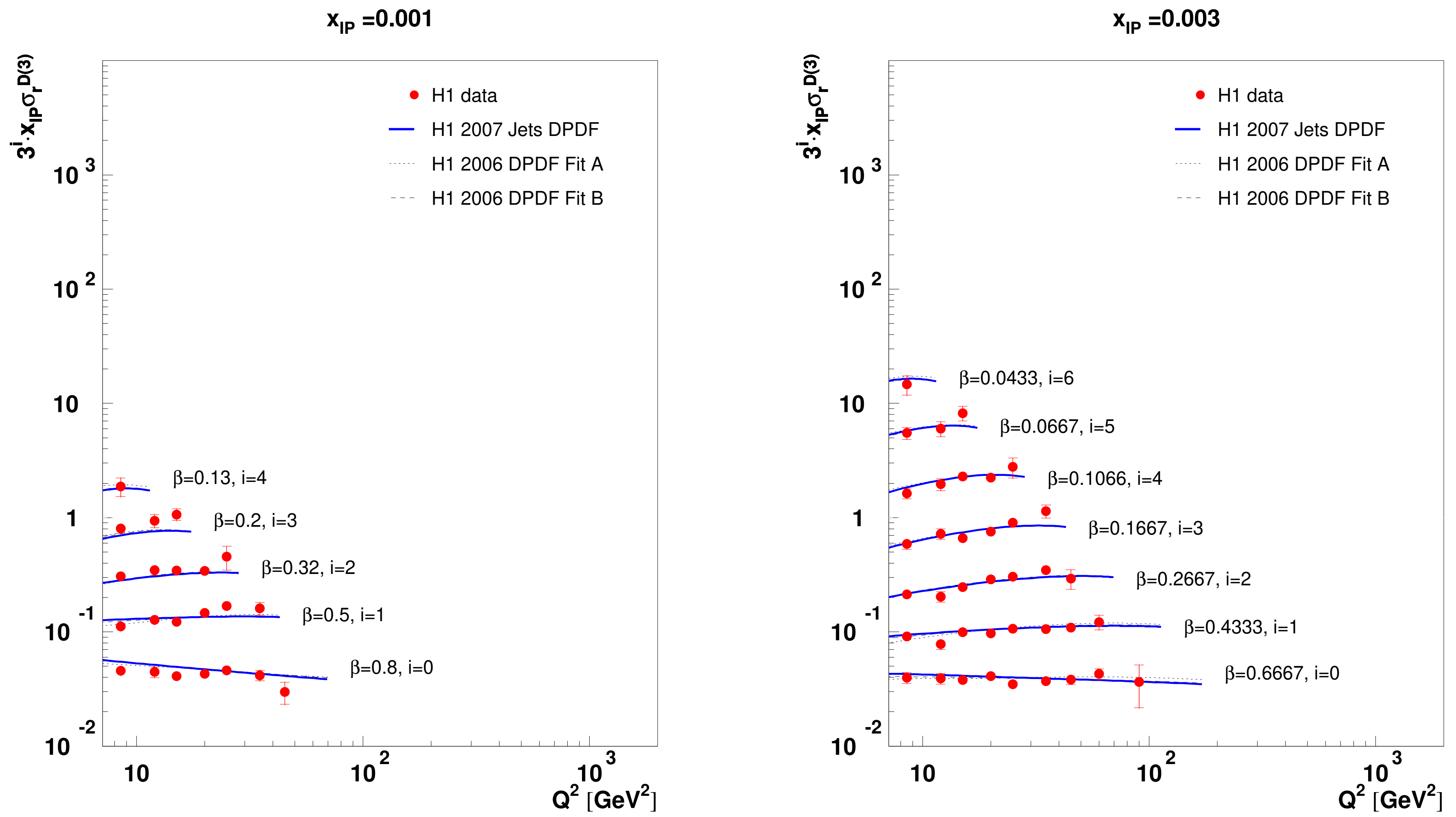

Figure 7: The Q^2 dependence of the diffractive reduced cross section $\sigma_r^{D(3)}$ multiplied by $x_{I\!P}$ at $x_{I\!P}$=0.001 (left) and $x_{I\!P}$=0.003 (right) at various values of β. The cross sections are multiplied by powers of 3 for better visibility. The data points are taken from the publication [5]. The inner and outer error bars on the data points represent the statistical and total uncertainties, respectively. Only data points included in the DPDF fits are shown. The data are compared to NLO QCD predictions based on the H1 2007 Jets DPDF, which are shown as solid lines. The dashed and dotted lines indicate the predictions of the H1 2006 DPDF fit A and B, respectively.

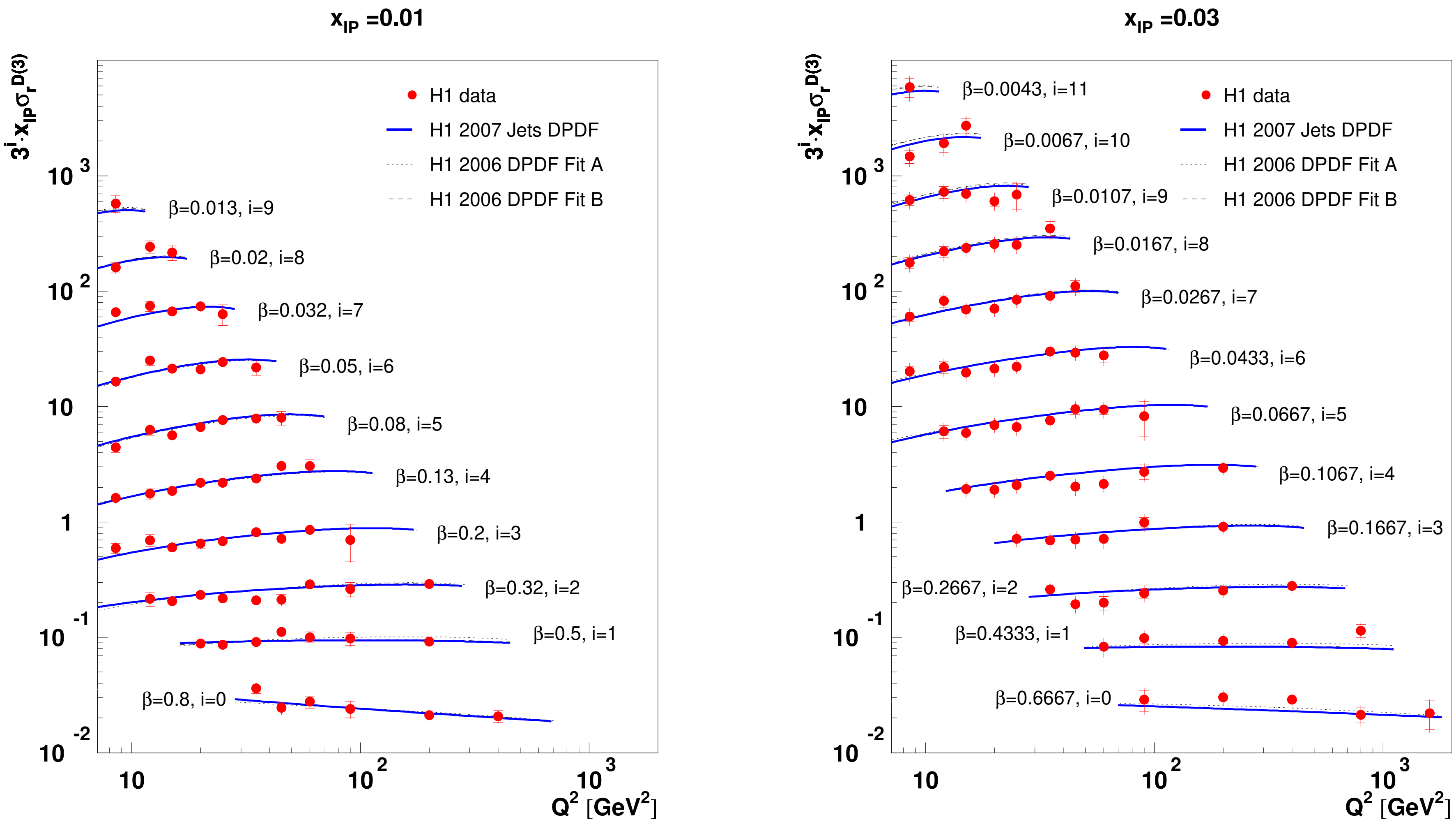

Figure 8: The Q^2 dependence of the diffractive reduced cross section $\sigma_r^{D(3)}$ multiplied by $x_{I\!P}$ at $x_{I\!P}$=0.01 (left) and $x_{I\!P}$=0.03 (right) at various values of β. See caption of figure 7 for further details.

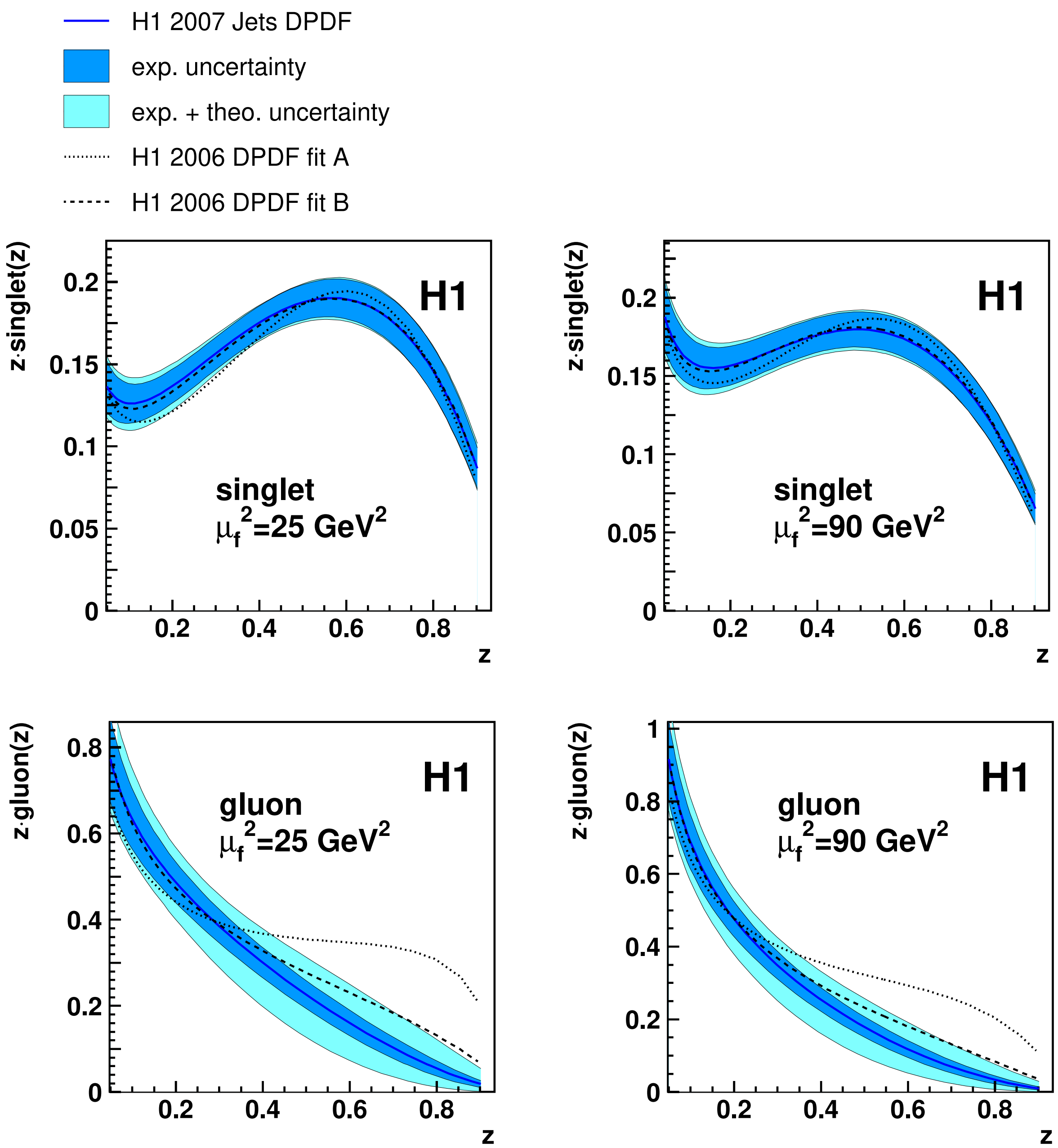

Figure 9: The diffractive quark density (top) and the diffractive gluon density (bottom) for two values of the squared factorisation scale μ_f^2: 25 GeV^2 (left) and 90 GeV^2 (right). The solid line indicates the H1 2007 Jets DPDF, surrounded by the experimental uncertainty (dark shaded band) and the experimental and theoretical uncertainties added in quadrature (light shaded band). The dotted and dashed lines show the parton densities corresponding to the H1 2006 fit A and fit B from [5], respectively.

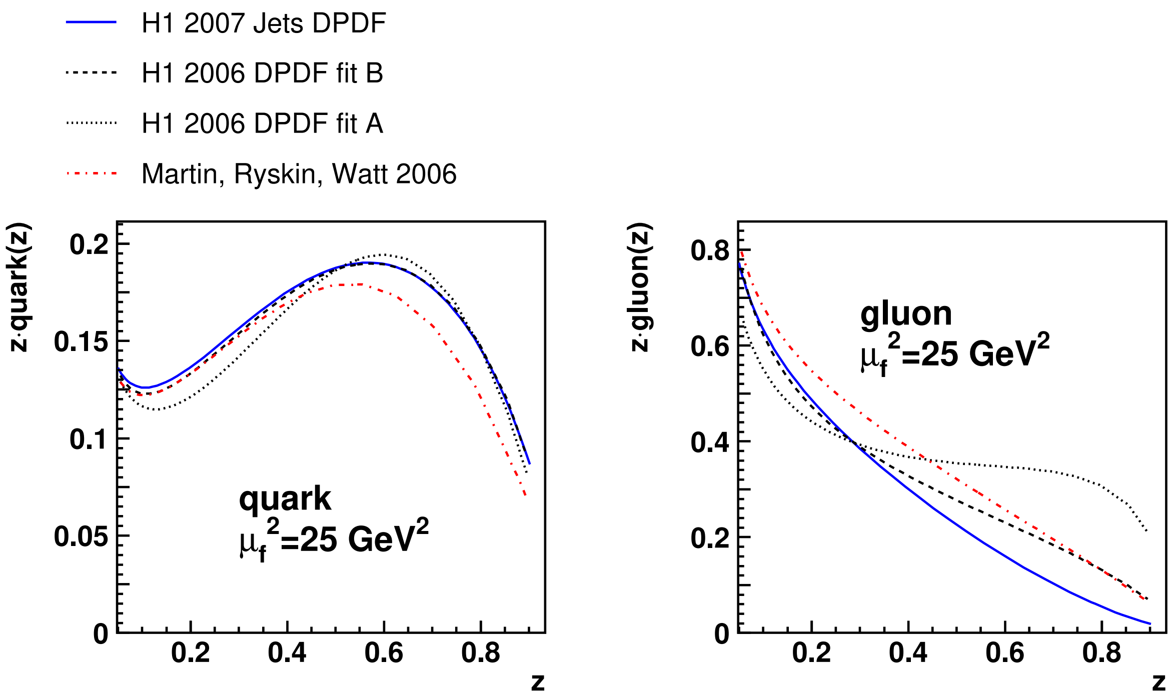

Figure 10: The diffractive quark density (left) and the diffractive gluon density (right) for the factorisation scale $\mu_f^2 = 25\ \mathrm{GeV}^2$. The solid line indicates the H1 2007 Jets DPDF. The dotted and dashed lines show the parton densities corresponding to the H1 2006 fit A and fit B from [5], respectively. The dashed-dotted line shows the DPDFs as determined by Martin, Ryskin and Watt in [15].

$\log(x_{I\!P})$	$d\sigma/d\log(x_{I\!P})$ [pb]	$\delta_{\rm tot.}$ [pb]	$\delta_{\rm stat.}$ [pb]	$\delta_{\rm uncorr.}$ [pb]	$\delta_{\rm corr.}$ [pb]	hadr. corr.
-2.3 - -2.2	11.8	3.0	2.1	1.5	1.4	1.55 $\pm$ 0.15
-2.2 - -2.1	16.8	3.4	2.4	1.9	1.5	1.38 $\pm$ 0.02
-2.1 - -2.0	35.0	6.5	4.6	3.6	2.9	1.24 $\pm$ 0.02
-2.0 - -1.9	49.6	7.8	4.3	3.7	5.3	1.24 $\pm$ 0.04
-1.9 - -1.8	66.8	8.2	4.9	4.2	4.9	1.10 $\pm$ 0.06
-1.8 - -1.7	96	14	6	8	9	1.11 $\pm$ 0.04
-1.7 - -1.6	125	20	7	10	16	1.04 $\pm$ 0.13
-1.6 - -1.5	110	23	7	6	21	1.04 $\pm$ 0.06

Table 4: Bin averaged differential cross sections of diffractive dijet production at the hadron level (corrected to the QED Born level) and the corresponding uncertainties as a function of $x_{I\!P}$. The corrections applied to the NLO prediction for hadronisation and the associated uncertainty are also given.

y	$d\sigma/dy$ [pb]	$\delta_{\rm tot.}$ [pb]	$\delta_{\rm stat.}$ [pb]	$\delta_{\rm uncorr.}$ [pb]	$\delta_{\rm corr.}$ [pb]	hadr. corr.
0.1 - 0.16	57	11	6	5	8	1.16 $\pm$ 0.14
0.16 - 0.22	117	20	10	7	16	1.09 $\pm$ 0.03
0.22 - 0.28	125	18	9	6	13	1.10 $\pm$ 0.02
0.28 - 0.34	123	18	9	8	14	1.09 $\pm$ 0.07
0.34 - 0.40	92	15	8	6	12	1.10 $\pm$ 0.10
0.40 - 0.46	92	14	7	6	10	1.12 $\pm$ 0.01
0.46 - 0.52	79	13	7	7	9	1.13 $\pm$ 0.15
0.52 - 0.58	70	12	7	5	8	1.11 $\pm$ 0.14
0.58 - 0.64	63	14	6	6	10	1.11 $\pm$ 0.12
0.64 - 0.7	52	11	6	6	7	1.11 $\pm$ 0.10

Table 5: Bin averaged differential cross sections of diffractive dijet production at the hadron level (corrected to the QED Born level) and the corresponding uncertainties as a function of y. The corrections applied to the NLO prediction for hadronisation and the associated uncertainty are also given.

$z_{I\!P}$	$d\sigma/dz_{I\!P}$ [pb]	$\delta_{\mathrm{tot.}}$ [pb]	$\delta_{\mathrm{stat.}}$ [pb]	$\delta_{\mathrm{uncorr.}}$ [pb]	$\delta_{\mathrm{corr.}}$ [pb]	hadr. corr.
0.0 - 0.1	6.0	2.2	1.4	0.7	1.6	1.28 ± 0.18
0.1 - 0.2	79	16	6	7	13	1.09 ± 0.10
0.2 - 0.3	100	16	6	7	13	1.10 ± 0.06
0.3 - 0.4	95	14	6	5	11	1.08 ± 0.03
0.4 - 0.5	82	12	6	4	9	1.11 ± 0.03
0.5 - 0.6	65.5	9.2	4.8	4.0	6.8	1.12 ± 0.01
0.6 - 0.7	42.6	5.2	3.7	1.8	3.1	1.09 ± 0.09
0.7 - 0.8	25.3	4.0	2.8	2.0	2.0	0.99 ± 0.28
0.8 - 0.9	13.7	4.5	2.7	2.4	2.7	0.90 ± 0.32
0.9 - 1.0	11.4	4.2	3.5	1.9	1.3	–

Table 6: Bin averaged differential cross sections of diffractive dijet production at the hadron level (corrected to the QED Born level) and the corresponding uncertainties as a function of $z_{I\!P}$. The corrections applied to the NLO prediction for hadronisation and the associated uncertainty are also given. No hadronisation correction is given for the highest $z_{I\!P}$ bin since it cannot be evaluated reliably.

$p^{\star}_{T,jet1}$ [GeV]	$d\sigma/dp^{\star}_{T,jet1}$ [pb/GeV]	$\delta_{\mathrm{tot.}}$ [pb/GeV]	$\delta_{\mathrm{stat.}}$ [pb/GeV]	$\delta_{\mathrm{uncorr.}}$ [pb/GeV]	$\delta_{\mathrm{corr.}}$ [pb/GeV]	hadr. corr.
5.5 - 6.5	21.2	3.0	1.0	1.6	2.3	1.09 ± 0.12
6.5 - 7.5	15.0	2.2	0.8	1.0	1.8	1.11 ± 0.06
7.5 - 9.0	7.0	1.0	0.4	0.4	0.8	1.11 ± 0.01
9.0 - 11.0	2.18	0.38	0.19	0.19	0.26	1.17 ± 0.15
11.0 - 13.5	0.38	0.088	0.062	0.028	0.056	1.12 ± 0.08

Table 7: Bin averaged differential cross sections of diffractive dijet production at the hadron level (corrected to the QED Born level) and the corresponding uncertainties as a function of $p^{\star}_{T,jet1}$. The corrections applied to the NLO prediction for hadronisation and the associated uncertainty are also given.

$\Delta\eta^{\star}_{jets}$	$d\sigma/d\Delta\eta^{\star}_{jets}$ [pb]	$\delta_{\mathrm{tot.}}$ [pb]	$\delta_{\mathrm{stat.}}$ [pb]	$\delta_{\mathrm{uncorr.}}$ [pb]	$\delta_{\mathrm{corr.}}$ [pb]	hadr. corr.
0 - 0.257	44.8	6.6	2.6	3.4	5.0	1.05 ± 0.05
0.257 - 0.514	46.6	6.0	2.8	2.4	4.7	1.11 ± 0.01
0.514 - 0.771	32.5	4.6	2.3	1.5	3.7	1.12 ± 0.04
0.771 - 1.029	29.3	4.6	2.1	1.5	3.8	1.14 ± 0.10
1.029 - 1.286	20.3	3.5	1.9	1.6	2.4	1.15 ± 0.03
1.286 - 1.543	12.1	2.2	1.3	0.8	1.7	1.20 ± 0.13
1.543 - 1.8	8.4	1.6	1.1	0.6	1.1	1.10 ± 0.14

Table 8: Bin averaged differential cross sections of diffractive dijet production at the hadron level (corrected to the QED Born level) and the corresponding uncertainties as a function of $\Delta\eta^{\star}_{jets}$. The corrections applied to the NLO prediction for hadronisation and the associated uncertainty are also given.

$z_{I\!P}$	$d^2\sigma/dz_{I\!P}d\mu^2$ [pb/GeV^2]	$\delta_{\rm tot.}$ [pb/GeV^2]	$\delta_{\rm stat.}$ [pb/GeV^2]	$\delta_{\rm uncorr.}$ [pb/GeV^2]	$\delta_{\rm corr.}$ [pb/GeV^2]	hadr. corr.
$29\ \mathrm{GeV}^2 < Q^2 + p^2_{T,jet1} < 50\ \mathrm{GeV}^2$						
0.0 - 0.1	0.16	0.10	0.05	0.04	0.07	1.32 ± 0.04
0.1 - 0.2	1.10	0.30	0.15	0.18	0.19	0.99 ± 0.35
0.2 - 0.3	1.24	0.25	0.17	0.10	0.15	1.09 ± 0.11
0.3 - 0.4	1.16	0.24	0.17	0.07	0.15	0.97 ± 0.14
0.4 - 0.5	1.12	0.23	0.18	0.06	0.13	1.08 ± 0.01
0.5 - 0.6	0.61	0.17	0.10	0.07	0.11	1.11 ± 0.10
0.6 - 0.7	0.45	0.12	0.09	0.05	0.06	0.91 ± 0.01
0.7 - 0.8	0.197	0.071	0.056	0.031	0.030	0.86 ± 0.60
0.8 - 0.9	0.042	0.036	0.022	0.024	0.015	0.98 ± 0.50
0.9 - 1.0	0.22	0.22	0.18	0.09	0.09	–
$50\ \mathrm{GeV}^2 < Q^2 + p^2_{T,jet1} < 70\ \mathrm{GeV}^2$						
0.0 - 0.1	0.124	0.059	0.047	0.018	0.030	1.21 ± 0.70
0.1 - 0.2	1.52	0.32	0.18	0.11	0.25	1.10 ± 0.10
0.2 - 0.3	1.91	0.34	0.20	0.15	0.23	1.08 ± 0.12
0.3 - 0.4	1.54	0.33	0.17	0.14	0.25	1.14 ± 0.02
0.4 - 0.5	1.18	0.23	0.15	0.09	0.15	1.07 ± 0.20
0.5 - 0.6	1.09	0.23	0.15	0.08	0.15	1.08 ± 0.12
0.6 - 0.7	0.74	0.15	0.12	0.05	0.07	1.13 ± 0.08
0.7 - 0.8	0.35	0.12	0.08	0.05	0.06	0.92 ± 0.36
0.8 - 0.9	0.20	0.13	0.09	0.07	0.06	0.76 ± 0.65
0.9 - 1.0	0.11	0.13	0.07	0.02	0.10	–

Table 9: Bin averaged double differential cross sections of diffractive dijet production at the hadron level (corrected to the QED Born level) and the corresponding uncertainties as a function of $z_{I\!P}$ in different bins of $\mu^2 = Q^2 + p^2_{T,jet1}$. The corrections applied to the NLO prediction for hadronisation and the associated uncertainty are also given. No hadronisation correction is given for the highest $z_{I\!P}$ bin since it cannot be evaluated reliably.

$z_{I\!P}$	$d^2\sigma/dz_{I\!P}d\mu^2$ [pb/GeV^2]	$\delta_{\mathrm{tot.}}$ [pb/GeV^2]	$\delta_{\mathrm{stat.}}$ [pb/GeV^2]	$\delta_{\mathrm{uncorr.}}$ [pb/GeV^2]	$\delta_{\mathrm{corr.}}$ [pb/GeV^2]	hadr. corr.
$70\ \mathrm{GeV}^2 < Q^2 + p^2_{T,jet1} < 100\ \mathrm{GeV}^2$						
0.0 - 0.1	0.0096	0.0083	0.0069	0.0036	0.0028	1.27 ± 0.47
0.1 - 0.2	0.66	0.15	0.09	0.04	0.11	1.13 ± 0.01
0.2 - 0.3	0.76	0.17	0.09	0.07	0.12	1.11 ± 0.08
0.3 - 0.4	0.78	0.14	0.09	0.06	0.10	1.05 ± 0.10
0.4 - 0.5	0.69	0.13	0.09	0.04	0.081	1.12 ± 0.05
0.5 - 0.6	0.66	0.11	0.09	0.05	0.069	1.17 ± 0.04
0.6 - 0.7	0.354	0.075	0.058	0.025	0.041	1.11 ± 0.04
0.7 - 0.8	0.261	0.063	0.051	0.022	0.028	1.07 ± 0.38
0.8 - 0.9	0.129	0.047	0.035	0.011	0.029	0.86 ± 0.30
0.9 - 1.0	0.106	0.074	0.057	0.037	0.030	–
$100\ \mathrm{GeV}^2 < Q^2 + p^2_{T,jet1} < 200\ \mathrm{GeV}^2$						
$z_{I\!P}$	$d^2\sigma/dz_{I\!P}d\mu^2$ [pb/GeV^2]	$\delta_{\mathrm{tot.}}$ [pb/GeV^2]	$\delta_{\mathrm{stat.}}$ [pb/GeV^2]	$\delta_{\mathrm{uncorr.}}$ [pb/GeV^2]	$\delta_{\mathrm{corr.}}$ [pb/GeV^2]	hadr. corr.
0.0 - 0.1	0.0	-	-	-	-	–
0.1 - 0.2	0.054	0.022	0.016	0.005	0.014	1.30 ± 0.12
0.2 - 0.3	0.128	0.036	0.022	0.015	0.025	1.16 ± 0.01
0.3 - 0.4	0.160	0.036	0.023	0.011	0.025	1.16 ± 0.05
0.4 - 0.5	0.150	0.039	0.023	0.018	0.026	1.16 ± 0.03
0.5 - 0.6	0.105	0.024	0.018	0.010	0.011	1.14 ± 0.01
0.6 - 0.7	0.075	0.016	0.013	0.004	0.006	1.13 ± 0.04
0.7 - 0.8	0.058	0.014	0.012	0.005	0.005	1.05 ± 0.28
0.8 - 0.9	0.052	0.015	0.013	0.005	0.005	1.01 ± 0.21
0.9 - 1.0	0.025	0.015	0.013	0.005	0.005	–

Table 10: Bin averaged double differential cross sections of diffractive dijet production at the hadron level (corrected to the QED Born level) and the corresponding uncertainties as a function of $z_{I\!P}$ in different bins of $\mu^2 = Q^2 + p^2_{T,jet1}$. The corrections applied to the NLO prediction for hadronisation and the associated uncertainty are also given. No hadronisation correction is given for the highest $z_{I\!P}$ bin since it cannot be evaluated reliably.